https://doi.org/10.5194/egusphere-2026-4745
Preprint. Discussion started: 10 September 2026

Observation of dark brown carbon in urban aerosols and its contribution to surface dimming

Yuezhi (August) Li[1,7†], Ganesh S. Chelluboyina[1†], Taveen S. Kapoor[1], Joseph V. Puthussery[1,6], Joshin Kumar[1], Guodong Ren[2], Jordan A. Hachtel[4], Zezhen Cheng[3], Nurun N. Lata[3], Gregory W. Vandergrift[3], Benjamin J. Sumlin[1], Chenchong Zhang[5], Dishit P. Ghumra[1], Swarup China[3], Rohan Mishra[2], Rajan K. Chakrabarty[1]

[1]Department of Energy, Environmental, and Chemical Engineering, Washington University in St. Louis; St. Louis, MO 63130, USA.

[2]Institute of Materials Science & Engineering, and Department of Mechanical Engineering and Materials Science, Washington University in St. Louis; St. Louis, MO 63130, USA.

[3]Environmental Molecular Sciences Laboratory, Pacific Northwest National Laboratory; Richland, WA 99354, USA.

[4]Oak Ridge National Laboratory, 1 Bethel Valley Road, Oak Ridge, TN 37830, USA.

[5]Department of Earth System Science, Stanford University, Stanford, CA 94305, USA.

[6]Department of Civil Engineering, Indian Institute of Technology Delhi, New Delhi, Delhi 110016, India.

[7]Department of Occupational and Environmental Health, College of Public Health, University of Iowa, Iowa City, IA 52242, USA.

[†]These authors contributed equally to this work.

Correspondence to: Rajan K. Chakrabarty (chakrabarty@wustl.edu)

Abstract. Dark brown carbon (d-BrC) aerosols are commonly associated with biomass burning and wildfire emissions, yet their occurrence and climatic impacts in urban environments remain elusive. Southeast Texas–a hub for petrochemical industries at the intersection of continental and marine airmasses–is strongly influenced by aerosol-induced surface dimming and extreme meteorological events. Here, the in-situ photoacoustic measurements reveal that over 80% of aerosol light absorption at blue and near-infrared wavelengths is due to non-black carbon (BC) aerosols. The computer-controlled scanning electron microscopy and particle-scale electron energy loss spectroscopy demonstrates the presence of refractory d-BrC in the coastal urban atmosphere as an absorption contributor. The diurnal pattern of BC and non-BC absorption suggests association of the non-BC aerosols such as d-BrC particles with local non-biomass burning combustion sources, potentially including traffic, flares, and industrial activities. Observationally constrained radiative-transfer calculations show that d-BrC contributes 40% of daytime-mean surface dimming and 50% of the total top-of-atmosphere radiative forcing attributable to light-absorbing carbon. Such radiative changes that influence local meteorology may also impact ~25% of the global population residing in coastal urban regions like Houston. Our findings demonstrate the presence and climatic importance of d-BrC in a coastal

https://doi.org/10.5194/egusphere-2026-4745
Preprint. Discussion started: 10 September 2026

urban environment in addition to wildfire plumes, highlighting the need for incorporation of d-BrC in aerosol-climate models.

https://doi.org/10.5194/egusphere-2026-4745
Preprint. Discussion started: 10 September 2026

1. Introduction

Aerosols are potent short-lived climate forcers that alter the Earth's radiative budget (Intergovernmental Panel On Climate Change, 2023), making them essential components of climate models. They impose a negative or positive atmospheric forcing depending on whether they are predominantly scattering or absorbing, respectively. Light-absorbing aerosols increase the net incoming shortwave radiation at the top-of-the-atmosphere (I_{TOA}^{net}) by changing the energy absorption distribution within the vertical atmosphere column: through increasing the atmospheric (A_{atm}) absorption component while reducing absorption at the surface (Schwarz et al., 2020) (A_{sfc}). This energy redistribution results in enhanced atmospheric heating and the diminishing of downwelling solar radiation reaching the surface, a phenomenon termed surface dimming (Ramanathan and Carmichael, 2008). Surface dimming by aerosols stabilizes the planetary boundary layer and thereby suppresses convection, which is associated with changes in precipitation pattern, frequency, and intensity. This is of particular concern in regions strongly influenced by mixed emission sources like urban areas (Andrews et al., 2010).

Coastal urban environments, home to 25% of the global population (Cosby et al., 2024; MacManus et al., 2021), are constantly exposed to a combination of aerosol emissions from diverse anthropogenic sources, such as industries and maritime shipping (Duarte and Duarte, 2020; Jensen et al., 2022), and natural sources, such as marine biogenic emissions (Jensen et al., 2025). The Southeastern Texas area, including the metropolitan Houston city, is greatly affected by aerosol-induced surface dimming, which further induces severe local meteorological turbulences (Andrews et al., 2010; Jensen et al., 2022; Zhang et al., 2018). Due to the high density of population affected by the well-mixed coastal urban air masses, it is necessary to holistically assess how the mixed emissions shape the aerosol optical properties and thereby the associated climate impacts.

Carbonaceous aerosols, including black carbon (BC) and brown carbon (BrC) (Andreae and Gelencsér, 2006), are major urban climate concerns because of their strong light absorption. BC is strongly light-absorbing across the ultraviolet-visible-infrared (UV-Vis-IR) spectrum (Bond et al., 2013), characterized by a mean imaginary refractive index (k) of 0.79. In contrast, the absorption properties of BrC are highly wavelength dependent across the short visible spectrum, with k values ranging from 10^{-4} to 10^{-1} that are several orders of magnitude lower than those of BC (Andreae and Gelencsér, 2006; Saleh, 2020; Sand et al., 2021).

https://doi.org/10.5194/egusphere-2026-4745
Preprint. Discussion started: 10 September 2026

To estimate the atmospheric radiative forcing of BrC aerosols on regional and global bases, researchers rely on aerosol-climate models, which bear large uncertainties mainly due to the wide range of optical properties and emission sources of BrC. Typically, climate models limit BrC absorption to UV and blue wavelengths (Andreae and Gelencsér, 2006; Sand et al., 2021). However, in biomass burning and wildfire plumes, recent laboratory and field studies (Atwi et al., 2022; Chakrabarty et al., 2023; Saleh et al., 2014) have observed strongly absorptive BrC ($k > 0.1$), or dark BrC (d-BrC). Unlike conventional BrC, the d-BrC exhibits high absorptivity at visible and near-IR wavelengths comparable to BC. This resemblance between d-BrC and BC absorption properties poses more challenges to the accurate estimation of BrC radiative impacts.

Current climate models, informed by emissions inventories, attribute BC as the dominant light absorber in urban environments (Moosmüller et al., 2009) and BrC in wildfire and biomass burning emissions (Zeng et al., 2020). However, field campaigns have consistently reported contributions of BrC from non-biomass burning emissions in major cities such as Los Angeles (Zhang et al., 2011) and Beijing (Yan et al., 2017). During the ACE-Asia field campaign, the mass of non-biomass organic carbon (OC) aerosols was 5–12 times higher than that of biomass burning OC aerosols across coastal and maritime sites in East Asia (Simoneit et al., 2004), while, in Houston, this ratio was 8 (Fig. 1a) (Al-Naiema et al., 2018). Moreover, the ACE-Asia campaign detected non-biomass d-BrC aerosols from ship engine exhaust, with a mean k value of 0.27 at 550 nm (Alexander et al., 2008; Corbin et al., 2019). Collectively, these observations hint at the presence of d-BrC in urban environments, potentially associated with non-biomass emissions. Nevertheless, observations of d-BrC in urban environments remain limited, and its optical characteristics and climatic impacts in urban settings have not been comprehensively analyzed (Alexander et al., 2008; Corbin et al., 2019). Therefore, there remains uncertainties in estimating the radiative impacts of BrC, particularly d-BrC, in urban environments.

Here, we present ensemble- and particle-scale measurements of light absorption, morphology, and chemical composition of brown carbon (BrC) aerosols in a coastal urban region of southeastern Texas during August 2022 as part of the TRacking Aerosol Convection interactions ExpeRiment (TRACER) field campaign, organized by the U.S. Department of Energy's Atmospheric Radiation Measurement (ARM) user facility. Our analyses demonstrate that d-BrC is present in a coastal urban environment and is a potential contributor to urban aerosol light absorption. Based on the observed d-BrC optical properties, we investigated the resulting shortwave radiative impacts including surface

https://doi.org/10.5194/egusphere-2026-4745
Preprint. Discussion started: 10 September 2026

dimming. The preceding TexAQS field study in the same region observed surface dimming twice as large as modeled, indicating underestimation of modelled aerosol light absorption (Fig. 1b) (Fast et al., 2006). These observations point to light-absorbing aerosol components unaccounted for in urban environments that contribute to surface dimming. Inclusion of the detected d-BrC absorption helps bridge this gap between modeled and measured aerosol radiative impacts. While d-BrC from biomass burning exerts a global-scale positive radiative forcing comparable to BC (Wang et al., 2025), the regional effects urban d-BrC, such as surface dimming, were previously less well-known and are demonstrated in this study.

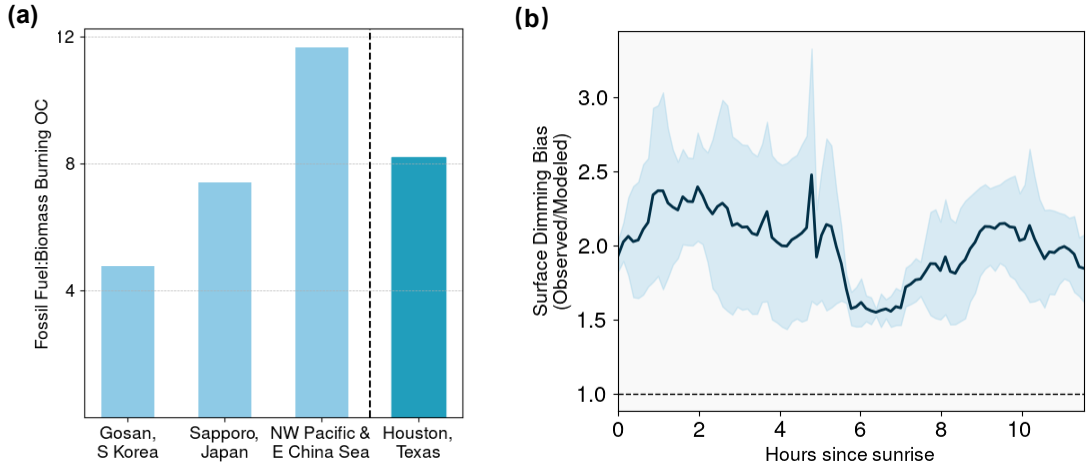

Figure 1. Present understanding of carbonaceous aerosol sources and uncertainty in their dimming potentials. **(a)** Abundance of fossil fuel emitted organic carbon (OC) in coastal urban regions. Fossil fuel to biomass burning OC median mass ratios, derived from compound source groups, for various East Asian sites and Houston ranges from 4 to 12. All these sites are either coastal or marine. East Asian sites are from the ACE-Asia field campaign (Simoneit et al., 2004), while Houston data is from Al-Naiema et al., 2018 (Al-Naiema et al., 2018). (b) Variation of surface dimming bias with hours elapsed since sunrise (approximately 07:00 local time) in La Porte. Bias is the average ratio of observational to modeled surface dimming and includes the standard deviation of four days of data (adapted from Fast et al. (Fast et al., 2006)).

https://doi.org/10.5194/egusphere-2026-4745
Preprint. Discussion started: 10 September 2026

2. Methods

2.1. Field Campaign Site and Instruments

The TRacking Aerosol Convection interactions ExpeRiment (TRACER) field campaign was hosted by Atmospheric Radiation Measurements (ARM) of the United States Department of Energy (DOE). The first ARM Mobile Facility (AMF1), as the main sampling site, was located next to the La Porte Municipal Airport (29°40'12.0" N, 95°0'26.9" W) in La Porte, Texas. During the field campaign, our instruments were deployed in the ARM guest trailer (Fig. A1 in Appendix A). We sampled the ambient aerosol particles through a PM2.5 cyclone inlet ~8 meters above the ground. Three integrated photoacoustic nephelometers (IPN) measured the real-time aerosol light absorption and scattering coefficients at wavelengths of 405, 721, and 1047 nm. Particle samples were also collected on 47-mm PTFE and quartz fiber membrane filters and on transmission electron microscope (TEM) grids using a time-resolved aerosol collector (TRAC) for offline analyses. After collection, the filter samples were stored at -20°C and the grid samples were stored at room temperature until further analysis. Silica diffusion dryers were attached to remove excess moisture in aerosol samples before they reached the instruments. Silica gel in the diffusion dryers was replaced by regenerated gel every two days to ensure continuous effectiveness. In this study, we also used the refractory black carbon (rBC) mass concentration measured by ARM's single particle soot photometer (SP2), deployed in the Aerosol Observing System (AOS) trailer next to the ARM guest trailer at AMF1 (Fig. A1). The data were downloaded from the ARM Data Discovery website (https://adc.arm.gov/discovery/#/results).

2.2. Integrated Photoacoustic Nephelometer (IPN)

The design and working principles of IPN, also known as the photoacoustic spectrophotometer (PAS), were elaborated in previous work (Arnott et al., 1999). Briefly, in contrast to filter-based optical instruments, IPN is an in-situ first-principle instrument that measures aerosol light absorption of airborne particles. The instrument uses a pulsed laser to illuminate sampled particles, transforming light energy into thermal energy. The illuminated particles then release thermal energy as heat, causing expansion of the surrounding air as pressure waves that can be detected as acoustic signals. The photoacoustic cell is designed to be coupled with Helmholtz resonators for amplifying acoustic signals. A microphone captures and transmits the signals to a computer that converts them into light absorption coefficients (b_{abs}) based on the photoacoustic spectrum. Aerosol light scattering and extinction are also measured by two photodiode sensors installed at the middle and end, respectively, of the photoacoustic cell.

https://doi.org/10.5194/egusphere-2026-4745
Preprint. Discussion started: 10 September 2026

At AMF1, the IPNs were operated at 1-liter-per-minute flowrate to measure b_{abs} at 405, 721, and 1047 nm with a 2-second resolution. An autozero calibration with filtered particle-free air was performed after every 200 measurements. The collocated ARM SP2 measured rBC mass concentration at a 1-Hz resolution. All raw data were converted to hourly means, and the data points below detection limits (< 10 ng/m^3 for SP2) were filtered out before performing further calculations. The subsequent analysis in this study focuses on data collected in August 2022 to avoid the interference of Saharan dust events in July. The 721-nm IPN measurements were not included because the instrument encountered laser issues during the field campaign, outputting ~78% of missing data.

2.3. Estimating Non-BC Absorption

The light absorption from non-BC aerosol components ($b_{abs,non\text{-}BC}$) was calculated by subtracting BC absorption ($b_{abs,BC}$) from the total absorption ($b_{abs,TOT}$) measured using the IPNs (Eqn (1)).

$$b_{abs,non-BC} = b_{abs,TOT} - b_{abs,BC} \quad (1)$$

The $b_{abs,BC}$ was converted from SP2-measured rBC mass concentration ($[BC]_{SP2}$) by multiplying it to the theoretical BC mass absorption cross-section (Beeler and Chakrabarty, 2021) (MAC_{BC}) at 550 nm of 11.25 m^2/g (Eqn. 2). A multiplicative factor (f) (Wu et al., 2018) of 1.5 ± 0.48 was incorporated to account for absorption enhancement due to the lensing effect from coatings on BC (Beeler and Chakrabarty, 2021).

$$b_{abs,BC}(\lambda = 550\,nm) = f \cdot [BC]_{SP2} \cdot \mathrm{MAC}_{BC}(\lambda = 550\,nm) \quad (2)$$

Using a BC absorption Ångström exponent ($AÅE_{BC}$) ranging from 0.6 to 1.3 (Kirchstetter et al., 2004), the $b_{abs,BC}$ at 550 nm was extrapolated to 405 and 1047 nm (Eqn (3)).

$$b_{abs,BC}(\lambda) = b_{abs,BC}(550) \cdot \left(\frac{\lambda}{550\,nm}\right)^{-\mathrm{AÅE}_{BC}} \quad (3)$$

With the measured $b_{abs,TOT}$ from IPN and the calculated $b_{abs,BC}$ from SP2 at wavelengths of interest, the non-BC light absorption, $b_{abs,non\text{-}BC}$, was obtained as the difference between $b_{abs,TOT}$ and $b_{abs,BC}$.

2.4. Solvent-Extraction Ultraviolet-Visible (UV-Vis) Spectrophotometry

At the AMF1 site, aerosols were sampled on 47-mm PTFE Teflon membrane filters (polypropylene, 1 µm, Whatman™). Each filter was sampled for 72 hours with an air flow rate of 18 L min^{-1}. After sampling, the filters were

https://doi.org/10.5194/egusphere-2026-4745
Preprint. Discussion started: 10 September 2026

placed into filter-storage petri dishes, which were sealed using parafilm and wrapped using aluminum foil, and stored under -20°C.

Pieces with area of 25 mm^2 were cut from five particle-laden PTFE filters and extracted separately in 4 mL of water and 4 mL of acetonitrile (ACN) followed by 1-hour sonication. Insoluble particles were filtered out by passing the extracts through Teflon membrane syringe filters (polytetrafluoroethylene, 0.22 µm, Fisherbrand). The extracts were analyzed using a UV-Vis spectrophotometer (LAMBDA 365, PerkinElmer) to measure the percentage of light transmittance ($\%Tr(\lambda)$) and thereby the absorbance ($A(\lambda)$) of soluble BrC from 300 to 800 nm with a 1-nm resolution (Eqn (4)).

$$A(\lambda) = 2 - \log_{10}\left(\%Tr(\lambda)\right) \quad (4)$$

The solvent-based BrC light absorption coefficient ($b_{abs,sol}$) can then be determined using Eqn (5):

$$b_{abs,sol}(\lambda) = \left(A(\lambda) - A(700)\right)\frac{V_L}{V_a \cdot l} \times \ln(10) \quad (5)$$

where V_L is volume of the solvents, V_a is the volume of air sampled through the filter cut area, and l is the optical length travelled by the UV-Vis light beam (1 cm). The logarithmic factor was multiplied to convert $A(\lambda)$ from base 10 to natural logarithm. To account for the signal drift, all absorbance measurements were normalized to absorbance at 700 nm ($A(700)$). The complex part of imaginary refractive index for the solvent extracted BrC (k_{BrC}) can then be derived (Eqn (6)).

$$k_{BrC}(\lambda) = \frac{\rho\lambda\left(b_{abs,sol}(\lambda)/m_{BrC}\right)}{4\pi} \quad (6)$$

where ρ is the BrC density (Chakrabarty et al., 2023) (1.4 g/cm^3) in the solvents and $b_{abs,sol}(\lambda)/m_{BrC}$ represents the BrC mass absorption efficiency as the ratio between $b_{abs,sol}$ and extracted BrC mass concentration.

2.5. Thermal Optical Carbon (OC-EC) Analysis

In parallel with PTFE filters, particle samples were collected on prebaked 47-mm quartz-fiber membrane filters (PALLFLEX® Tissuquartz™) with a flow rate of 42 L min^{-1}, each for 72 hours. An organic-and-elemental-carbon (OC-EC) analyzer (M5L, Sunset Laboratory Inc.), operated based on the thermal-optical technique, was used to detect the mass concentration OC and EC (Birch and Cary, 1996) per unit area on the filter. Since the area of filter punch and

https://doi.org/10.5194/egusphere-2026-4745
Preprint. Discussion started: 10 September 2026

the sampling flowrate were known, the measured mass concentration per unit area can be converted into the equivalent volumetric mass concentration in the ambient.

First, a 1.5-cm^2 particle-laden quartz filter punch (one from each of the eight collected samples) is placed onto the glass cartridge and inserted into the sample oven under a laser beam. We followed the National Institute for Occupational Safety and Health (NIOSH) 5040 protocol for the analysis which proceeds in three stages. Stage 1 removes all OC on the filter by increasing temperature in 4 steps in oxygen-free argon gas. The high temperature (500-700 ºC) decomposes inorganic carbonates, pyrolyzes up to 30% of OC into EC, and vaporizes the rest of OC. The pyrolysis process was monitored by measuring laser transmission through the filter. The vaporized OC is oxidized in an oxidizer oven into carbon dioxide (CO_2), which is carried by argon to the methanator oven and reduced to methane. A flame ionization detector (FID) detects the methane. In stage 2, the sample oven is cooled to 525 ºC, and 2% oxygen/argon gas mixture is injected. Through stepped increase in temperature to 850 ºC, all original EC and the EC from OC pyrolysis would be oxidized to CO_2 and then methane. In stage 3, standard methane gas with a known volume is used to obtain a calibration curve, based on which the FID and laser transmission data can be used to calculate EC and OC mass per unit filter area (µg cm^{-2}). With known sampling flow rate and duration, the ambient mass concentration (µg m^{-3}) of EC and OC can be determined. The OC-EC analyzer can detect OC ranging from 0.2 to 600 µg cm^{-2} and EC ranging from 0.2 to 30 µg cm^{-2}, with a detection limit of 0.1 µg cm^{-2}. Different OC species (OC1, OC2, OC3, OC4, and pyrolyzed OC) are identified from the OC peaks at different temperatures. In terms of volatility, OC1 is considered to consist primarily of intermediate-volatility organic compounds (IVOC) and semi-VOC (SVOC); OC2 and OC3 combined corresponds to low-VOC (LVOC); and OC4 represents extremely-low-VOC (ELVOC) (Ma et al., 2016).

2.6. Scanning Transmission Electron Microscopy with Electron Energy Loss Spectroscopy (STEM-EELS)

Aerosol particles were sampled onto Formvar/carbon supported copper grids and lacey carbon supported copper grids using the TRAC. Details of working principles and design of the TRAC are described in Laskin et al. (Laskin et al., 2003a). Briefly, it samples particles through a 0.46-mm jet nozzle at a 0.8-0.9 lpm flow rate, rendering an effective cutoff particle size (d_{50}) of 0.36-0.38 µm. During the campaign, each grid sampled for 25 minutes and was later used for offline electron microscopy analyses.

https://doi.org/10.5194/egusphere-2026-4745
Preprint. Discussion started: 10 September 2026

Four lacey carbon grids were analyzed using a scanning transmission electron microscopy (STEM) with electron energy loss spectroscopy (STEM-EELS) fitted with a Nion spectrometer coupled with a Dectris ELA high-speed electron-counting detector at the Oak Ridge National Laboratory. The STEM was operated at an accelerating voltage of 60 kV with a probe convergence of 30 mrad. The spectrometer collected the EEL spectrum at a 25 mrad angle with a dispersion of 20 meV channel^{-1}. The EELS datasets were acquired as spectrum images, containing approximately 70 × 70 pixels (pixel size of 1-3 nm), with a dwell time of ~50 ms/pixel and a total acquisition time of ~5 min for each dataset. The zero-loss peak (ZLP) obtained after monochromation for all EELS datasets had a full width at half maximum of about 100–150 meV. To remove surface contaminants, the grids were heated to 150 ℃ in vacuum, equivalent to 465 ℃ under atmospheric pressure based on the Clausius-Clapeyron equation (Donahue et al., 2006), for 6 hours.

We derived particle-scale optical properties from the low-loss EEL spectra. A reflected-tail method was used to remove ZLP and its tail from the low-loss EEL spectra of carbonaceous particles (Zhu et al., 2014). To calculate the dielectric functions, we performed Kramers-Kronig analysis (KKA) using HyperSpy (De La Pena et al., 2017), an open-source Python software package for multi-dimensional data analysis. The KKA used fast-Fourier transform method (Egerton, 2009) within the thin-film approximation, in which the film thickness is estimated as the aerosol particle diameter (Egerton, 2009; Zhu et al., 2014). Yet, KKA fails for EEL spectra collection near the particle edge due to increase in contribution from surface plasmons. Derivation of dielectric function using this approach is valid for particles larger than 50 nm when the low-loss EELS are collected at least 10 nm away from the edges. For smaller particles of 20-50 nm, low-loss EEL spectra collected close to the center can still be used to determine the refractive index. In this study, we used EELS data collected at the center of particles of all sizes.

The real part of dielectric function (Re[$1/\varepsilon(E)$]) was calculated from the imaginary part of energy-loss function (Im[$-1/\varepsilon(E)$]) via Eqn. 7, where E' is energy loss and P represents the Cauchy principal value. Equation (8) can then be used to calculate the dielectric function.

$$Re\left[\frac{1}{\varepsilon(E)}\right] = 1 - \frac{2}{\pi} P \int_0^\infty Im\left[\frac{-1}{\varepsilon(E')}\right] \frac{E' dE'}{E'^2 - E^2} \quad (7)$$

$$\varepsilon(E) = \varepsilon_1(E) + i\varepsilon_2(E) = \frac{Re[1/\varepsilon(E)] + iIm[-1/\varepsilon(E)]}{\{Re[1/\varepsilon(E)]\}^2 + \{Im[-1/\varepsilon(E)]\}^2} \quad (8)$$

https://doi.org/10.5194/egusphere-2026-4745
Preprint. Discussion started: 10 September 2026

The derived dielectric function can be used to determine the complex refractive index ($n + ik$), where n and k are the real and imaginary parts of refractive index, respectively, and i denotes the imaginary part of a function.

$$n = \left\{\frac{\left[\varepsilon_1^2 + \varepsilon_2^2\right]^{1/2} + \varepsilon_1}{2}\right\}^{1/2} \quad (9)$$

$$k = \left\{\frac{\left[\varepsilon_1^2 + \varepsilon_2^2\right]^{1/2} - \varepsilon_1}{2}\right\}^{1/2} \quad (10)$$

2.7. Radiative Forcing and Surface Dimming Modeling

The net top-of-atmosphere downwelling shortwave radiation (I_{TOA}^{net}) in W m^{-2} can be partitioned into the atmospheric (A_{atm}) and the surface (A_{sfc}) absorption components:

$$I_{TOA}^{net} = A_{atm} + A_{sfc} \quad (11)$$

This partitioning is rarely static. Aerosols perturb this energy balance, causing shortwave radiative forcing, which can be calculated by the change in each quantity. If this change is positive, the forcing is positive, and vice versa. This forcing is similarly partitioned between the atmosphere and the surface:

$$F_{TOA} = F_{atm} + F_{sfc} \quad (12)$$

In principle, most aerosols are concentrated in the lower atmosphere, so almost all of the atmospheric forcing is situated in that layer. By calculating the column energy balance for both pristine and aerosol conditions and comparing results from both, radiative forcing and surface dimming due to the aerosol can be inferred. These calculations are performed using the libRadtran uvspec program (Emde et al., 2016) for d-BrC and BC particles of varying concentrations within the planetary boundary layer (PBL), assumed to be at a height of 1 km. The range of planetary boundary layer heights was previously reported (Lamer et al., 2024) at the TRACER field campaign site in Houston as between 500 to 2000 m. For each layer, libRadtran, through two-stream radiative transfer calculations, determines the E_{net}, or the difference in irradiance between vertically downwards (direct+diffuse) and upwards (diffuse) directions. The forcing by the aerosol in the atmosphere is:

$$F_{atm} = \left[E_{net,1km}^{aerosol} - E_{net,1km}^{pristine}\right] - \left[E_{net,0km}^{aerosol} - E_{net,0km}^{pristine}\right] \quad (13)$$

The forcing at the surface is

https://doi.org/10.5194/egusphere-2026-4745
Preprint. Discussion started: 10 September 2026

$$F_{sfc} = E_{net,0km}^{aerosol} - E_{net,0km}^{pristine} \quad (14)$$

The top of atmosphere radiative forcing is similarly calculated and equals the sum of the above two forcings.

The dimming at the surface is calculated as

$$Dimming = E_{\downarrow,0km}^{aerosol} - E_{\downarrow,0km}^{pristine} = \frac{F_{sfc}}{1-\alpha} \quad (15)$$

where α is the surface albedo, taken to be 0.1, consistent with urban surfaces. Dimming is caused by aerosol extinction of the downward solar irradiance. The absorption contribution of this dimming can be calculated by setting the surface albedo to zero.

Simulations were constrained by d-BrC and BC observational data on optical properties and concentrations. The refractive index data based on EELS measured dielectric function was used to calculate the spectral single scatter albedo, extinction coefficient and moments of the phase function between 350-1200 nm at a resolution of 10 nm. Lorenz-Mie theory calculations were performed using the PyMieScatt python package (Sumlin et al., 2018). Mass concentrations of BC were found from OC-EC analysis of collected filter samples, from which number concentration can be determined assuming a lognormal distribution:

$$N = \frac{M}{\frac{\pi}{6}\rho_p d_{pg}^3 \exp\left(4.5\left(\ln \sigma_g\right)^2\right)} \quad (16)$$

which is ~10 particles/cc for BC. The calculations here showcase the relative dimming potentials of BC and d-BrC at the d-BrC:BC number concentration ratio derived from OC-EC analysis, and the absolute forcing and dimming values would scale depending upon actual abundance. For the calculations of optical properties, the following properties (Alexander et al., 2008; Bond et al., 2013; Chakrabarty et al., 2023) were used: ρ_{BC} = 1800 kg/m^3, $\rho_{d\text{-}BrC}$ = 1400 kg/m^3, σ_g = 1.6, d_{pg} = 215 nm for TRACER particles and d_{pg} = 230 nm for ACE-Asia particles.

The spectral energy balances at each layer boundary from libRadtran were numerically integrated across the full wavelength range to generate broadband instantaneous forcing values for each layer. Simulations were repeated across the day during August 22, 2022 at a temporal resolution of half an hour, and thereafter averaged to find the diurnal averaged forcing and dimming values.

https://doi.org/10.5194/egusphere-2026-4745
Preprint. Discussion started: 10 September 2026

As expected, for all species considered, the surface forcing and dimming were negative, and the atmospheric and TOA forcings were positive. TRACER d-BrC and BC are assumed to be externally mixed; this is likely true considering the independent existence of d-BrC and BC in wildfire emissions (Adachi et al., 2024) and therefore the forcings are additive at the concentrations observed. Regardless of their mixing state, the energy removed from the surface due to dimming is trapped in the PBL causing atmospheric warming.

https://doi.org/10.5194/egusphere-2026-4745
Preprint. Discussion started: 10 September 2026

3. Results and Discussion

3.1. Dominant Non-BC Light Absorption

The study site (AMF1) was located ~4 km south of the Houston Ship Channel, ~5 km northwest of the Galveston Bay coastline, and close to a myriad of industrial plants and major roadways (Fig. 2a). The aerosol light absorption was measured using IPNs operated at blue (405 nm) and near-IR (1047 nm) wavelengths. The absorption measurements were supplemented by rBC mass concentration measured using the collocated ARM's SP2 (Fig. A1). Based on these measurements, we calculated the BC light absorption and observed that a large fraction of aerosol absorption cannot be attributed to BC. The non-BC light-absorbing aerosol components contributed ~80% of the total absorption at 405 nm and ~88% at 1047 nm (Fig. 2b).

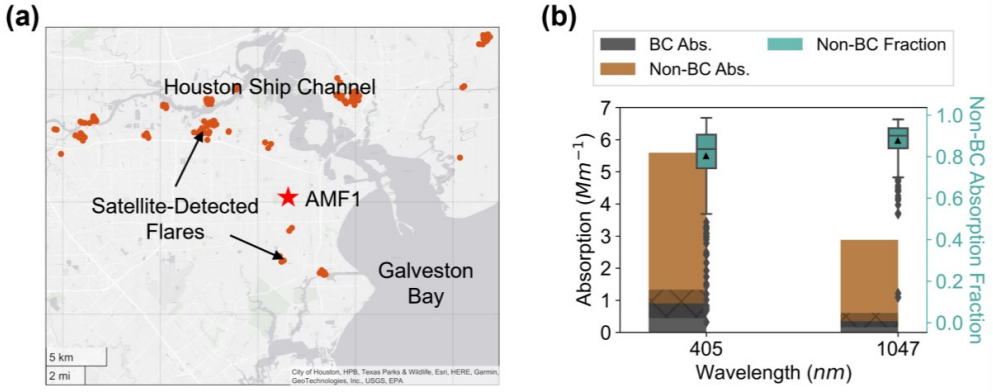

Figure 2. (a) Map showing locations of the main study site (red star) and the major emissions sources, including the Houston Ship Channel, the Galveston Bay, and flares indicating oil refineries or petrochemical industries. **(b)** Boxplots showing the distribution of BrC absorption fractions and stacked bar plots showing the mean BrC and BC absorption coefficients at 405 and 1047 nm, determined from SP2 and IPN measurements. The boxplots show the minimum (lower tips of the whisker), first quantile (lower bases of the box), median (horizontal solid lines inside the box), third quantile (upper bases of the box), maximum (upper tips of the whisker), and the outlier data (diamond markers). The black triangles overlapping the boxplots denote the mean non-BC absorption fraction based on the BC absorption enhancement factor of 1.5. The shaded areas on the stacked bar plots represent the uncertainties in the BC absorption coefficient, converted from the rBC mass concentration measured by SP2, incorporating the BC absorption enhancement factor of 1.5 ± 0.48 (Wu et al., 2018) and the BC absorption Ångström exponent of 0.6-1.3 (Kirchstetter et al., 2004).

Concurrent and collocated PTFE filter samples were extracted in water and ACN separately and analyzed using UV-Vis spectrophotometry. The soluble BrC contributes mainly to absorption at near-UV and blue wavelengths, while the ACN-soluble BrC exhibits additional absorption extending into the green and red wavelengths (Fig. 3a). The absorption properties of ACN-soluble BrC, including its mean imaginary refractive index at 550 nm (k_{550} = 0.0099) and absorption Ångström exponent ($AÅE_{365/550}$ = 4.92), fall within the range of moderately absorptive BrC detected in other urban regions worldwide (Boreddy et al., 2022; Lei et al., 2018; Zhang et al., 2013). This aligns with the strong short-wavelength absorption expected for BrC that is soluble in organic solvents (Saleh, 2020). However, the

https://doi.org/10.5194/egusphere-2026-4745
Preprint. Discussion started: 10 September 2026

298 ACN-soluble BrC in TRACER does not account for the observed near-IR non-BC absorption, suggesting additional
299 contributions from insoluble BrC components (Atwi et al., 2022). The quartz-fiber filter samples were subjected to
300 thermal-optical carbon analysis to retrieve the mass concentration and fractions of EC and OC. Low to extremely low
301 volatile OC (LVOC and ELVOC; ~37.5%) exceeded EC (~11%) by a factor of ~3.4 in mass concentration (Fig. 3b).
302 Given d-BrC's high absorptivity at near-IR wavelengths, low volatility, and insolubility in common organic solvents
303 (Atwi et al., 2022; Chakrabarty et al., 2023; Saleh, 2020; Saleh et al., 2018; Shetty et al., 2019), we hypothesize that
304 d-BrC is a contributor to the observed non-BC light absorption during the TRACER campaign.

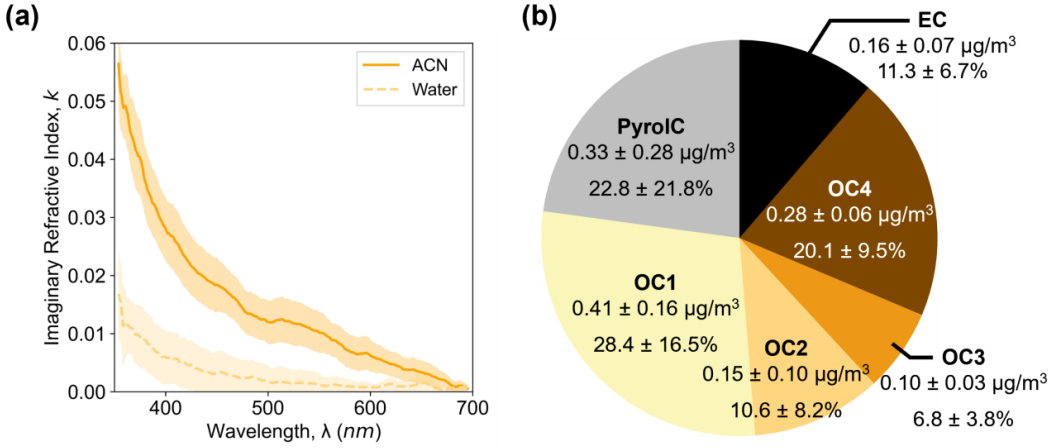

305 **Figure 3. (a)** Mean imaginary part (*k*) of the complex refractive index against optical wavelength (λ) for water and acetonitrile
306 (ACN) extracted BrC from the PTFE filter samples (n = 5), derived from the solvent-based UV-Vis spectrophotometry. The solid
307 and dashed lines represent the mean *k* values, and the shaded area denotes standard deviation. (**b)** Mass concentrations and fractions
308 of elemental carbon (EC) and organic carbon (OC) components detected on the quartz filter samples (n=8) using the thermal optical
309 carbon (OC-EC) analysis. Our analysis followed the National Institute for Occupational Safety and Health (NIOSH) protocol.

310 **3.2. Presence of d-BrC in Urban Atmosphere**

311 To validate our hypothesis, we examined the single-particle scale physicochemical and absorption properties of
312 TRACER aerosols using computer-controlled scanning electron microscopy coupled with coupled with energy-
313 dispersive X-ray spectrometry (CCSEM-EDX; described in detail in Appendix B) and STEM-EELS. Among >12000
314 particles scanned by CCSEM-EDX, over 40% of the particles were carbonaceous aerosols (Fig. B1a in Appendix B).
315 Under the SEM's low-pressure condition (2×10^{-5} – 3×10^{-6} Torr), a large fraction of organic particles retained dome-
316 like shapes (Figs. B1b-c), confirming that these particles consisted of low to extremely low-volatile organic
317 compounds (LVOC and ELVOC). The TRACER organic particles were also thermally stable, experiencing little
318 evaporation or morphology degradation up to 150 °C in the stage-heating environmental TEM (ETEM) (Fig. B2),
319 which translates to 465 °C under standard atmospheric conditions (Donahue et al., 2006).

https://doi.org/10.5194/egusphere-2026-4745
Preprint. Discussion started: 10 September 2026

For individual particles, STEM-EELS enabled direct retrieval of their dielectric functions (ε) between electron energy loss of 1 to 4.1 eV, from which the particles' imaginary (k) and real (n) refractive indices between 300 to 1200 nm wavelengths were derived. Fig. 4d shows the STEM image of a TRACER organic particle (named Particle 2 hereafter), along with its dielectric function (Fig. 4e) and refractive index (Fig. 4f). Particle 2 exhibits high spectral absorptivity, with k equal 0.1387 at visible 550 nm and 0.0833 at near-IR 1047 nm, accompanied by an $AÅE_{365/550}$ value of 1.78 and relatively constant spectral n values. While the optical properties of Particle 2 are close to those of a TRACER soot particle (k_{550} = 0.1743; k_{1047} = 0.1477; $AÅE_{365/550}$ = 1.49) shown in Fig. C1 in Appendix C, its morphology distinguishes it from aggregated soot BC, and its submicron size excludes the possibility of it being char BC (Corbin et al., 2019). These optical characteristics ($k_{550} > 0.1$; $2.5 > AÅE_{365/550} > 1.5$), low to extremely low volatility, and submicron, amorphous morphology corroborate that Particle 2 is consisted primarily of strongly absorbing d-BrC (Chakrabarty et al., 2023; Saleh, 2020; Saleh et al., 2014). This demonstrates that d-BrC aerosols are present in the coastal urban atmosphere at La Porte. Fig. 4g shows another TRACER organic particle (Particle 3) with low to extremely low volatility, yet it is less absorbing (k_{550} = 0.0725; k_{1047} = 0.0298) than the d-BrC Particle 2, despite that its wavelength dependence feature ($AÅE_{365/550}$ = 2.13) falls within the range of d-BrC, as shown in Figs. 4h-i.

https://doi.org/10.5194/egusphere-2026-4745
Preprint. Discussion started: 10 September 2026

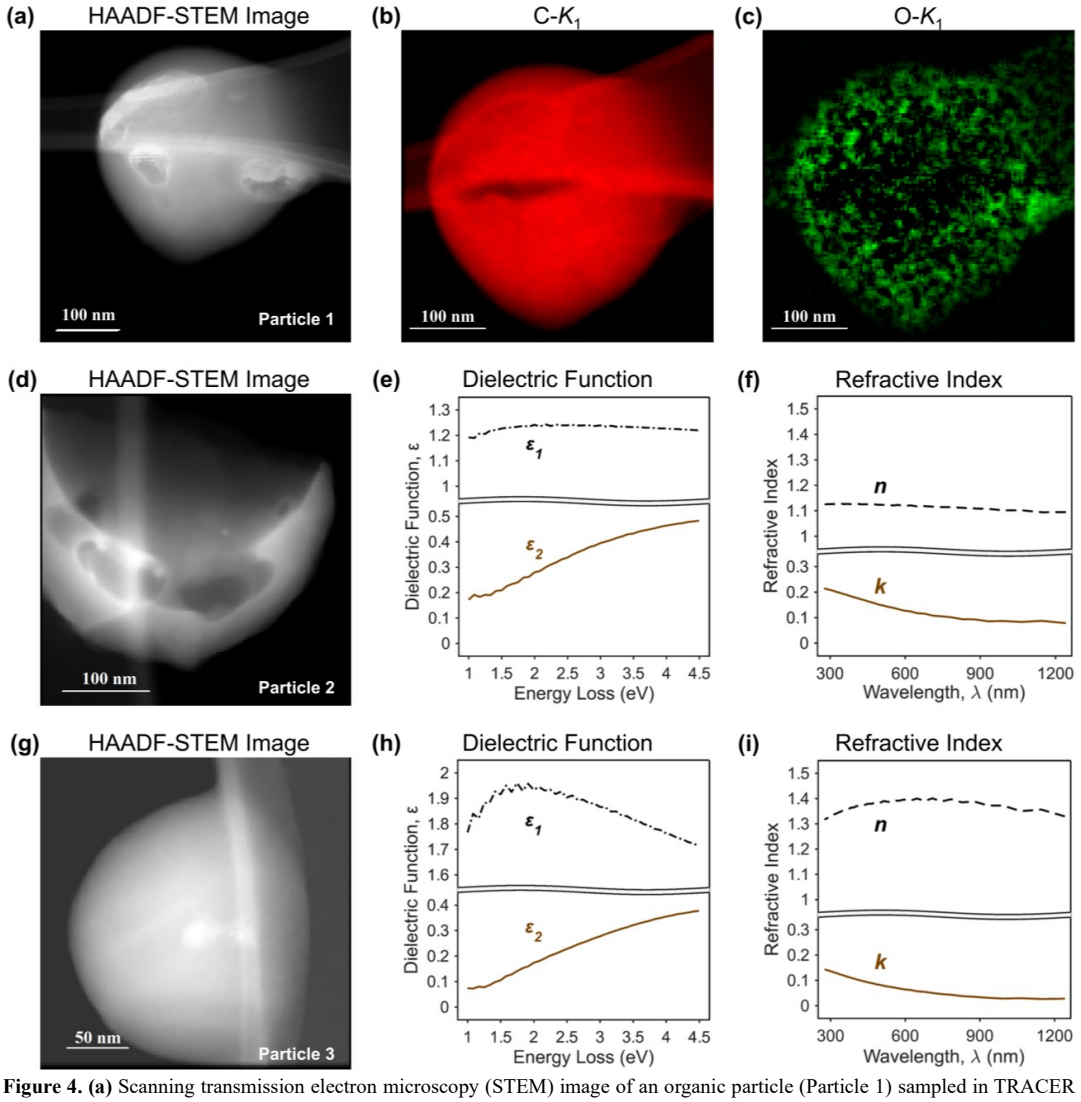

Figure 4. (a) Scanning transmission electron microscopy (STEM) image of an organic particle (Particle 1) sampled in TRACER campaign, acquired simultaneously with the electron energy loss spectroscopy (EELS), with its single-particle elemental composition scan showing the distribution of **(b)** carbon and **(c)** oxygen within the particle. **(d, g)** STEM images of BrC particles (Particle 2 and Particle 3) sampled in TRACER campaign. The real (ε_1) and imaginary (ε_2) part of the dielectric function of **(e)** Particle 2 and **(h)** Particle 3, determined using low-loss EELS, plotted against electron energy-loss level ranging from 1 to 4 eV. The real (n) and imaginary (k) part of the complex refractive index of **(f)** Particle 2 and **(i)** Particle 3, derived from their dielectric function, plotted against optical wavelength ranging from 300 to 1200 nm.

https://doi.org/10.5194/egusphere-2026-4745
Preprint. Discussion started: 10 September 2026

3.3. Possible Source of Urban d-BrC Aerosols

Several laboratory and field studies have reported d-BrC in biomass burning and wildfire emissions (Adler et al., 2019; Atwi et al., 2022; Chakrabarty et al., 2023; Hoffer et al., 2016, 2017; Saleh et al., 2014). The TRACER d-BrC and wildfire d-BrC share characteristics such as strong spectral absorptivity, low volatility, insolubility, and thermal stability (Chakrabarty et al., 2023; Saleh, 2020) with the TRACER d-BrC. The d-BrC aerosols have been hypothesized to be primary particles formed from heat-induced carbonization along with BC in high-temperature flames (Chakrabarty et al., 2023; Corbin and Gysel-Beer, 2019; Idrobo and Zhou, 2017). Following the methodology used in Chakrabarty et al. (Chakrabarty et al., 2023), we investigated the bonding characteristics of the TRACER d-BrC from the low-loss STEM-EELS measurements (Fig. 5a). Similar to wildfire d-BrC, the TRACER d-BrC showed a broadened π peak relative to the concurrently collected soot samples and the reference single-layer graphene (Idrobo and Zhou, 2017), consistent with the characteristics for co-emission of primary d-BrC and BC aerosols.

The diurnal variation of the TRACER BC and non-BC absorption at 405 nm during August 2022 showed synchronized morning and evening peaks (Fig. 5b), suggesting co-emission pattern of BC and non-BC aerosol components such as d-BrC consistent with local combustion sources, potentially including traffic (Farley et al., 2023) and flares and industrial activities (Guagenti et al., 2025). Nevertheless, we cannot exclude the possibility of long-range transport of biomass burning emissions since our available observations are insufficient for a definitive source apportionment of TRACER d-BrC.

https://doi.org/10.5194/egusphere-2026-4745
Preprint. Discussion started: 10 September 2026

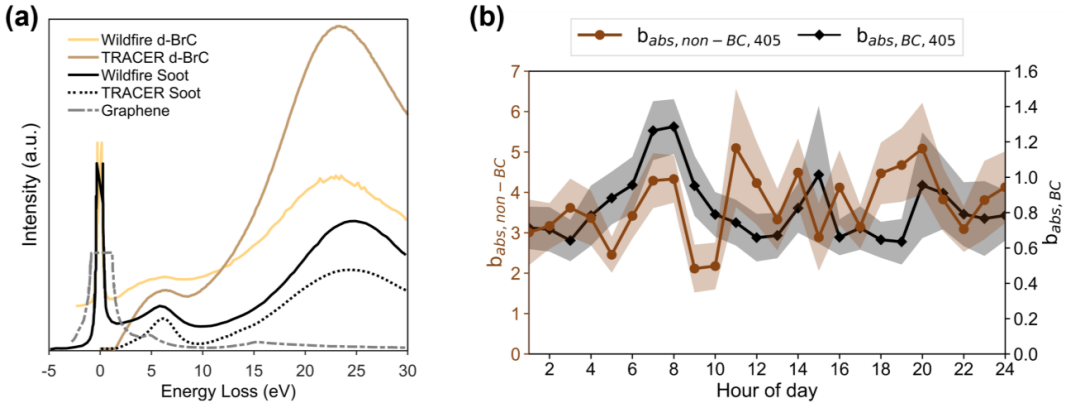

Figure 5. (a) The low-loss EEL spectra from 0 to 30 eV of the TRACER d-BrC compared with concurrent soot samples, wildfire d-BrC tar balls, and a reference single-layer graphene sample (Idrobo and Zhou, 2017). The π peak represents excitation of the π electron and broadens from graphene to soot and to d-BrC. This phenomenon is associated with reduced degree of graphitization and thereby fewer numbers of sp^2 hybridized carbon atoms from pure BC to d-BrC (Zhu et al., 2014), pointing to d-BrC formation via carbonization rather than graphitization along the BC formation pathway in high-temperature flames (Corbin and Gysel-Beer, 2019). The π+σ peak represents excitations of valence electrons, which shifts to higher electron energy loss from graphene to BrC (Idrobo and Zhou, 2017). **(b)** The mean diurnal variations of BC and BrC light absorption coefficient (b_{abs}) at 405 nm for the month of August. The primary y-axis (left) corresponds to BrC absorption (circular markers), and the secondary y-axis (right) corresponds to BC absorption (diamond markers). The shaded areas represent the standard error of mean for the corresponding absorption data. The 405-nm $b_{abs,BrC}$ include absorption from d-BrC and other less-absorbing BrC species.

3.4. Urban d-BrC Contribution to Surface Dimming and Boundary Layer Heating

D-BrC aerosol radiative impacts have not been as well documented as those of BC. Previous studies have extensively characterized total surface dimming (Wild, 2009), while attributing light absorption primarily to BC (Ramanathan and Carmichael, 2008). In Houston, based on Texas Air Quality Study (TexAQS II) *in situ* airborne measurements, refractory BC (rBC) daily-mean surface dimming was -3.3 W m^{-2}, but this excluded all other light-absorbing aerosols (Schwarz et al., 2009). In the Yellow Sea, total surface aerosol radiative forcing was -93.6 W m^{-2} AOD^{-1} in visible wavelengths (400-700 nm), but the contributions of different aerosol fractions were not known (Bush and Valero, 2003). Temporal variations in surface solar radiance (SSR) around the world have also been observed over decadal timespans, with aerosols being a key modulator (Wild, 2009). However, the precise partitioning of surface dimming among light-absorbing species co-emitted with BC, like d-BrC, remains poorly constrained.

To determine the radiative impact of d-BrC in the lower troposphere, we used the single-particle optical properties of TRACER d-BrC as inputs to run radiative transfer simulations in the atmospheric column using the libRadtran library (Emde et al., 2016). In comparison, BC was used as a reference to contextualize d-BrC's dimming potential. From the thermal-optical mass concentration data, we inferred a mean d-BrC-to-BC number concentration ratio of 2.3, ranging from 1.2 to 4.9, with the uncertainty arising from variability in the measured mass concentration of EC and OC

https://doi.org/10.5194/egusphere-2026-4745
Preprint. Discussion started: 10 September 2026

fractions. This contrasts to the ratio of 4 observed in wildfire smoke (Chakrabarty et al., 2023). We assumed that OC4, which is equivalent to ELVOC (Shetty et al., 2019), represents d-BrC, and EC represents soot BC (Corbin et al., 2019; Hoffer et al., 2017). A small fraction of EC may represent other forms of BC, such as char BC, thereby biasing the d-BrC-to-BC number concentration ratio low. The surface dimming in the shortwave spectrum (350-1200 nm) due to TRACER d-BrC is 0.51 W m^{-2} (ranging from 0.27 W m^{-2} to 1.08 W m^{-2}), two thirds of that due to co-emitted BC (0.76 W m^{-2}) (Fig. 6b). When the d-BrC-to-BC number concentration ratio exceeds 3.5, surface dimming due to TRACER d-BrC surpasses BC. The simulated contribution from d-BrC surface dimming could explain the two-fold discrepancy between observed and modeled surface dimming at La Porte during the previous TexAQS campaign, which also coincides with an underestimation of measured aerosol optical depth. Since the TOA RF due to TRACER d-BrC (+0.06 W m^{-2}) is the same as that due to BC (+0.06 W m^{-2}), TRACER d-BrC contributes half of total TOA RF due to light-absorbing carbon in the Houston area (Fig. 6a).

However, not all d-BrC emissions are alike across emission sources and geographies. At equal number concentrations, modeled surface dimming of d-BrC from East Asian ship engine exhaust is 2.9 times greater than the dimming due to TRACER d-BrC, owing to the relatively greater absorptivity of ship d-BrC. TRACER d-BrC and ship d-BrC also diverge in the fraction of surface dimming attributable to absorption, with absorption contributing 91% and 85% of the total surface dimming, respectively, and scattering accounting for the remainder. However, factoring in the real-world abundance ratios of these species, the magnitudes of their individual surface dimming are comparable. In the ACE-Asia campaign, the mass of refractory OC, of which d-BrC is a constituent, was ~0.85 to 1 times that of BC (Clarke et al., 2004), rendering a surface dimming effect of ship d-BrC (–0.64 W m^{-2}) comparable to that of BC (–0.76 W m^{-2}). During the TRACER campaign, although the d-BrC-to-BC mass concentration ratio was higher at 1.75, the relatively less absorbing d-BrC particles caused urban d-BrC dimming (–0.51 W m^{-2}) to also be comparable to that of BC. This highlights that both the specific fuel source of d-BrC and the number ratio relative to BC dictate the radiative impact of d-BrC.

https://doi.org/10.5194/egusphere-2026-4745
Preprint. Discussion started: 10 September 2026

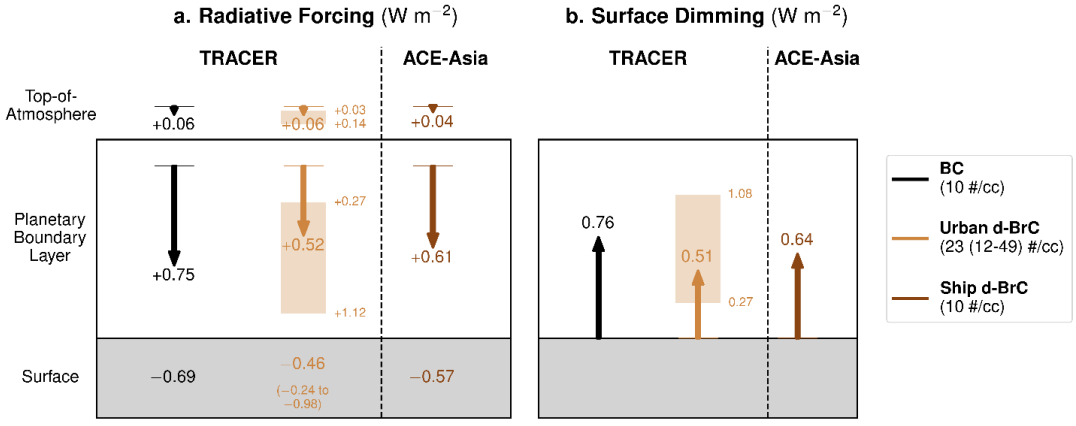

Fig. 6. Radiative forcing and surface dimming due to BC and d-BrC particles. Shortwave energy balance (W m^{-2}) in the atmospheric column is redistributed due to the presence of light-absorbing aerosols. Results show the radiative impact of BC and d-BrC detected in TRACER, with ship d-BrC from the ACE-Asia campaign in East Asia included for comparison. **a.** Radiative forcing and **b.** surface dimming are calculated for particles homogenously mixed in the lower tropospheric planetary boundary layer (PBL, 0-1 km), at specific number concentrations based on the observed ELVOC:EC mass concentration ratio. The range of d-BrC number concentrations arises from the bounding analysis based on measured mass variances for ELVOC and EC. Positive atmospheric RFs, denoted by the downward arrows, indicate an increase in absorption of shortwave energy over the baseline scenario (no aerosol in PBL). Negative RFs observed at the surface indicate a reduction from the baseline of shortwave energy absorbed by the ground. This reduction can be detected at the ground as a change in downward surface solar radiance (SSR) or surface dimming. The relationship between surface radiative forcing and surface dimming is a linear factor of 1/(1-α), where α is surface albedo.

https://doi.org/10.5194/egusphere-2026-4745
Preprint. Discussion started: 10 September 2026

3.5. Global Implications of Urban d-BrC

Based on their optical properties, BrC aerosols can be classified into very weakly (VW-BrC), weakly (W-BrC), moderately (M-BrC), and strongly absorptive (S-BrC) (Saleh, 2020), equivalent to d-BrC. From very weakly to strongly absorptive (Saleh, 2020), BrC exhibits gradually increasing absorptivity along the brown-black absorption continuum (Navinya et al., 2024), with BC being the evolutional endpoint on an optical basis (Saleh et al., 2018). As the most absorptive BrC species, d-BrC retains similar light absorption properties to BC (Bond et al., 2013; Chakrabarty et al., 2023), making it difficult to differentiate d-BrC and BC in light-absorption measurements (Bond et al., 2013; Chakrabarty et al., 2023). Consequently, accurate measurement and interpretation of aerosol optical properties are essential for climate models to estimate aerosols' impacts on Earth's radiative budget (Bond et al., 2013; Gliß et al., 2021).

Fig. 7 compares our results with the solvent-based BrC absorption properties measured in other urban areas worldwide (Bikkina et al., 2020; Boreddy et al., 2022; Huang et al., 2018; Kim et al., 2016; Laskin et al., 2015; Lei et al., 2018; Navinya et al., 2025; Rathod et al., 2024; Zhang et al., 2013). These studies measured BrC absorption properties using organic solvent extraction methods with UV-Vis spectrometry, categorizing BrC as either weakly (W-BrC) or moderately (M-BrC) absorptive. In this study, we coupled the UV-Vis analysis and STEM-EELS to derive both solvent-phase and particle-scale absorption Ångström exponent (AÅE) and k_{550} for TRACER BrC samples. For our samples, the ACN-soluble BrC was also classified as M-BrC. However, the absorption by d-BrC cannot be captured by the conventional solvent extraction methods, potentially underestimating the occurrence and absorption of d-BrC (Shetty et al., 2019), leading to systematic underrepresentation of d-BrC in both in-situ measurements and climate models. This highlights the need for recognizing d-BrC as an important light-absorbing aerosol component in urban

https://doi.org/10.5194/egusphere-2026-4745
Preprint. Discussion started: 10 September 2026

environments, in addition to its presence in biomass burning and wildfire plumes, and for incorporation of urban d-BrC into aerosol-climate models.

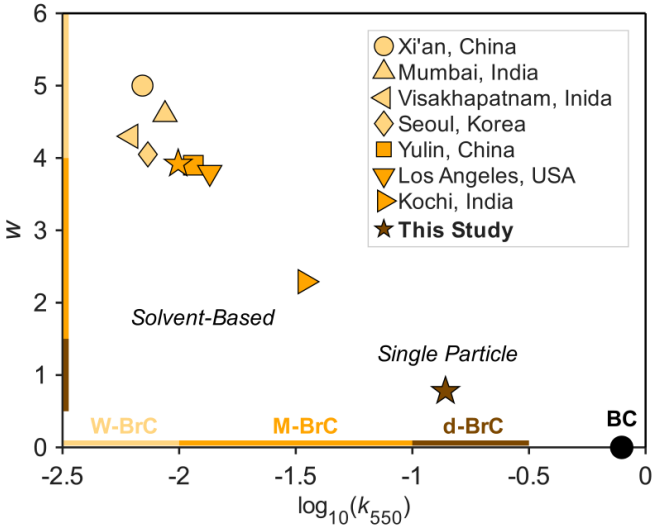

Fig. 7. Solvent-based optical methods underestimate BrC absorption. Plot of the absorption wavelength dependence (w = ÅAE – 1) against the logarithmic k_{550} values ($\log_{10}(k_{550})$) for BrC aerosols in different urban areas globally, including Los Angeles (Zhang et al., 2013) in the United States, Seoul (Kim et al., 2016) in South Korea, Xi'an (Huang et al., 2018) and Yulin (Lei et al., 2018) in China, and Mumbai (Rathod et al., 2024), Visakhapatnam (Bikkina et al., 2020), and Kochi (Boreddy et al., 2022) in India, based on previous studies where BrC samples were extracted in methanol. In this study, BrC was extracted using ACN. The datapoint for BC is shown as a reference.

Beyond the direct radiative effects, the impacts of d-BrC on atmospheric thermodynamics, including evaporation, convection, and cloud formation, also remain uncertain. Recent studies have shown contradicting conclusions for effects of Houston's polluted airmass on invigoration or suppression of cloud condensation nuclei (Al-Jabri et al., 2025; Thompson et al., 2025). Measurements from TRACER have revealed that ship emission particles are less hygroscopic than the surrounding marine background aerosol, reducing their ability to activate as cloud condensation nuclei by 69% (Thompson et al., 2025). Our radiative energy balance calculations for d-BrC point towards suppression of convection, with boundary layer heating (+1.46 W m^{-2}) triggering a thermodynamic stabilization of the column. Further investigations are necessary to constrain d-BrC's role in aerosol-convection interactions.

4. Conclusions

In conclusion, our results provide observational evidence for the presence of d-BrC aerosols in a coastal urban region in Southeast Texas. In-situ photoacoustic measurements showed that more than 80% of aerosol light absorption at blue and near-infrared wavelengths was attributable to non-BC absorption, while single-particle STEM-EELS identified

https://doi.org/10.5194/egusphere-2026-4745
Preprint. Discussion started: 10 September 2026

refractory strongly absorbing organic particles with optical properties consistent with d-BrC. Radiative transfer modeling showed that the light absorption and the potential abundance of d-BrC make it a more potent climate forcing agent than recognized in studies that neglect insoluble organic absorption (Bond et al., 2013). These observations and calculations collectively provide evidence for d-BrC aerosols as a climate-relevant concern not only in wildfire plumes but also in the urban atmosphere. Further, light absorption contribution from d-BrC has been underrepresented and attributed to BC in current measurements and models (Saleh et al., 2014), leading to underestimation in BrC radiative impacts.

Our direct observation of anthropogenic d-BrC with strong near-infrared absorption challenges this assumption, particularly in the context of recent observations highlighting the physical complexity of carbonaceous particles in urban environments. Recent analyses from the TRACER campaign have demonstrated that BC and other carbonaceous aerosols in the Houston urban plume exist in internally mixed states driven by intersecting marine and industrial air masses (Farley et al., 2024; Thompson et al., 2025). This internal mixing, particularly with secondary aerosols, enhances the mass absorption efficiency of BC, with the exact enhancement depending on coating morphology and refractive indices, which cannot be captured by a fixed AAE (Cheng et al., 2026). Because urban d-BrC and heavily coated, internally mixed BC share overlapping optical properties, standard optical differentiation methods are insufficient. This underscores the critical need to extend previous aerosol classification studies through particle-resolved optical characterizations, such as STEM-EELS utilized in this study, to accurately apportion light absorption in mixed urban environments.

However, several limitations should be considered when interpreting the results of this study. First, the non-BC absorption inferred from the difference between total and BC absorption should not be interpreted exclusively as d-BrC absorption. Other light-absorbing non-BC components may also contribute to the residual absorption. Moreover, the estimated BC absorption depends on theoretical MAC, absorption enhancement factor, and AÅE, with the uncertainties of these parameters propagating directly into the inferred non-BC absorption. Second, detailed particle-scale STEM-EELS characterization was conducted on a limited number of representative particles relative to the heterogeneous ambient aerosol population. Therefore, the measured particles may not fully capture the urban d-BrC abundance and diversity of composition and optical properties. In addition, the aerosols were sampled on filters and TEM grids. Particle collection, drying, storage, and subsequent sample treatments can alter the particle morphology

https://doi.org/10.5194/egusphere-2026-4745
Preprint. Discussion started: 10 September 2026

and composition, potentially causing differences between the measured particles and their original atmospheric state. Third, the diurnal aerosol absorption pattern does not permit definitive source apportionment of the observed d-BrC. Contributions from other sources such as long-range transport of biomass burning emissions cannot be excluded. More detailed source apportionment measurements like chemical tracers and concurrent measurements of air mass history would be required to quantitatively distinguish local from transported contributions. Fourth, in the surface dimming and boundary layer heating modeling, we used the mass concentration of OC4, or ELVOC, detected using thermal optical carbon analysis, as a proxy for the ambient TRACER d-BrC mass concentration. However, not all extremely low volatile BrC particles are d-BrC particles, as demonstrated by Particle 3 in Figs. 4g-i. Consequently, the modelled d-BrC climatic significance would potentially be overestimated. This urges for more comprehensive measurements capable of directly quantifying the mass, number concentration, size distribution, and optical properties of d-BrC to reduce this uncertainty. Fifth, the radiative transfer calculations involve several simplifying assumptions. Although the reported PBL height at the TRACER site varied from approximately 500 to 2000 m, the aerosols were assumed to be homogeneously distributed within a 1-km PBL. The calculations also rely on assumed particle size distributions, densities, and external mixing between d-BrC and BC. Variations in the vertical aerosol distribution, particle size, mixing state, and hygroscopic growth could therefore modify the calculated surface dimming and atmospheric heating. Finally, our observations were limited to August 2022 as a single coastal industrial site. Seasonal changes in emission sources, atmospheric processing, meteorology, and particle optical properties were not captured. Multi-season and multi-site observations are needed to determine the broader prevalence of urban d-BrC and to constrain its representation in regional and global climate models.

Despite these caveats, the results highlight a potentially important and previously underrepresented source of light absorption in urban atmospheres. The resemblance in the absorption strength, wavelength dependency, and single scattering albedo of d-BrC and BC complicates their differentiation in in-situ and remote sensing measurements (Bond et al., 2013; Chakrabarty et al., 2023), highlighting the importance of comprehensively understanding the absorption, physicochemical properties, and formation conditions of d-BrC in both wildfire and urban settings. Future studies combining direct measurements of d-BrC abundance and composition with source-specific tracers, multi-season observations, and vertically resolved aerosol measurements are needed to determine the prevalence, sources, atmospheric evolution, and geographical distributions of urban d-BrC. Incorporating these constraints into aerosol-

https://doi.org/10.5194/egusphere-2026-4745
Preprint. Discussion started: 10 September 2026

511 climate models (Navinya et al., 2024) will be essential for accurately assessing the broader contribution of urban d-
512 BrC to associated atmospheric heating, surface dimming, and radiative forcing at the regional and global scales.

https://doi.org/10.5194/egusphere-2026-4745
Preprint. Discussion started: 10 September 2026

513 **Appendix A: Instrument Setup at AMF1 of TRACER Field Campaign.**

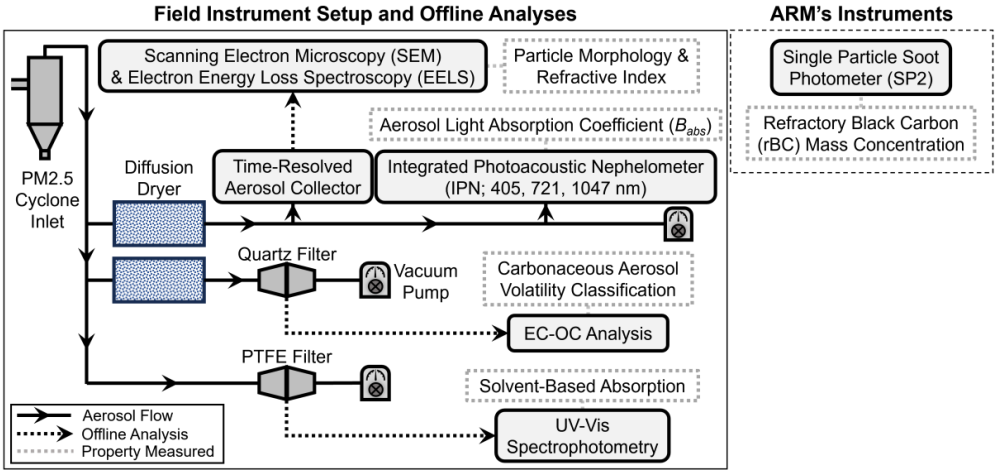

514 **Figure A1.** The schematic illustration of the instrument setup for real-time in-situ aerosol light absorption measurements and for
515 aerosol sample collection with their associated offline analyses. Ambient aerosols were sampled through a $PM_{2.5}$ cyclone inlet and
516 sent through a diffusion dryer to remove excess water content. The time-resolved aerosol collector (TRAC) and the integrated
517 photoacoustic nephelometers (IPNs) shared a common sampling line after a diffusion dryer. A 47-mm polytetrafluoroethylene
518 (PTFE)-membrane filter and a 47-mm quartz-fiber filter are in separate parallel sampling lines from the TRAC and IPN. No
519 diffusion dryer was deployed for the Teflon filters because of their waterproof nature; another diffusion dryer was attached before
520 the quartz filters to prevent water content from damaging the filters.

https://doi.org/10.5194/egusphere-2026-4745
Preprint. Discussion started: 10 September 2026

Appendix B: Electron Microscopy Analyses

In this study, 18 grids (>12000 particles) were analyzed under room temperature (293K) and near-vacuum condition (2×10^{-5} – 3×10^{-6} Torr) using the computer-controlled FEI Quanta digital field emission gun environmental scanning electron microscopy coupled with an energy dispersive X-ray spectrometer (CCSEM-EDX), operated at 20 kV voltage and 480 pA current. The near-vacuum condition in CCSEM evaporates and removes the volatile to semi-volatile organic compounds. SEM images of particle morphology upon deposition were obtained by observing the particles after tilting the substrates by 75° from horizontal plain. The chemical compositions of the sampled particles were analyzed using CCSEM-EDX, which measured the relatively weighted elemental percentages of C, N, O, Na, Mg, Al, Si, P, S, Cl, K, Ca, Mn, Fe, Cu, and Zn and the aera-equivalent diameters for each particle. The ultrathin carbon film renders low background carbon signal, enabling the automated CCSEM-EDX analysis in identifying deposited particles and scanning for their detailed elemental compositions (Laskin et al., 2003b). Based on the elemental spectrum for each particle scanned, the CCSEM classified the particles into "Na-rich" (sea salt), "Na-rich/Sulfate" (inorganic sulfates), "Sulfate", "Carbonaceous", "Dust", and "Other" categories. Within the sodium-containing particles ([Na > 0]), those that contain more sodium than any other detectable metals and sulfur ([Na] > [S]) are "Na-rich" particles. If the sodium content in the particles is less than sulfur ([Na] < [S]) but still more than the other detectable metals, they are classified as "Na-rich/Sulfate". The "Dust" particles have more detectable metals, such as aluminum, silicone, calcium, iron, manganese, and zinc, than sodium (sum[Al, Si, Ca, Fe, Mn, Zn] > [Na]). The "carbonaceous" and "sulfate" particles belong to sodium-free particles ([Na] = 0). If the particles only contain carbon (C), nitrogen (N), and oxygen (O) elements, it is considered as "Carbonaceous". If, in addition to C, N, and O, the particles only contain S, they are categorized as "Sulfates". All remaining particles that do not fit into any specified categories are assigned to the "Other" group (Fig. B1). The carbonaceous particles were dominant (40.1%) for most particle sizes, and Na-rich and sulfate-rich particles also account for large fractions (22.6% and 23.5%, respectively).

An environmental transmission electron microscopy (ETEM) was also used to examine the particles samples with stepped heating from room temperature (20 °C) to 150 °C under low pressure (Fig. B2), equivalent to ~140 to ~465 °C under standard atmospheric conditions. Temperatures in a vacuum can be converted to equivalent temperatures under atmospheric pressure according to the Clausius-Clapeyron equation (Donahue et al., 2006).

https://doi.org/10.5194/egusphere-2026-4745
Preprint. Discussion started: 10 September 2026

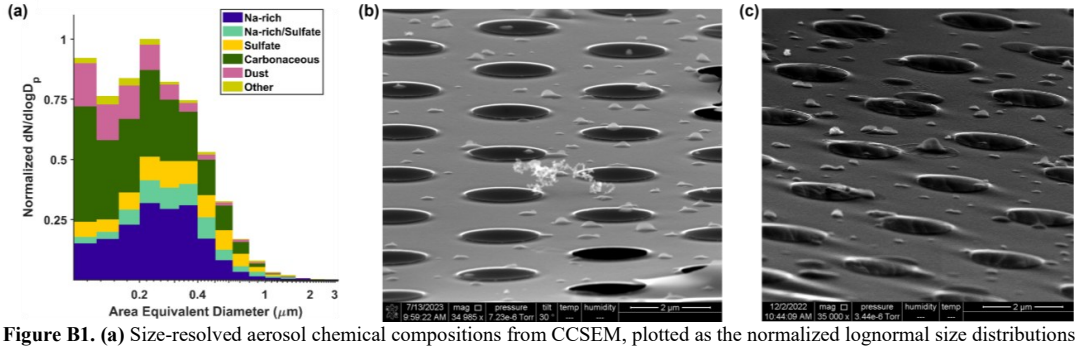

Figure B1. (a) Size-resolved aerosol chemical compositions from CCSEM, plotted as the normalized lognormal size distributions ($dN/d\log(d_p)$) against the area equivalent particle diameter in μm. **(b, c)** Tilted scanning electron microscopy (SEM) image showing abundant ELVOC particles that retained dome-shaped morphology without evaporation under vacuum conditions in the SEM.

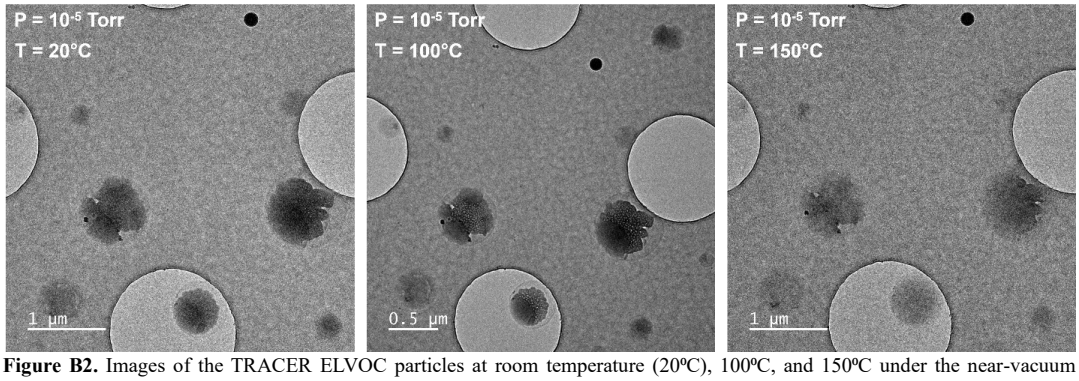

Figure B2. Images of the TRACER ELVOC particles at room temperature (20ºC), 100ºC, and 150ºC under the near-vacuum condition in the environmental transmission electron microscopy (ETEM). The particles exhibited no obvious evaporation or morphological changes until the temperature reached 150ºC.

https://doi.org/10.5194/egusphere-2026-4745
Preprint. Discussion started: 10 September 2026

Appendix C: EELS Scanned Particles

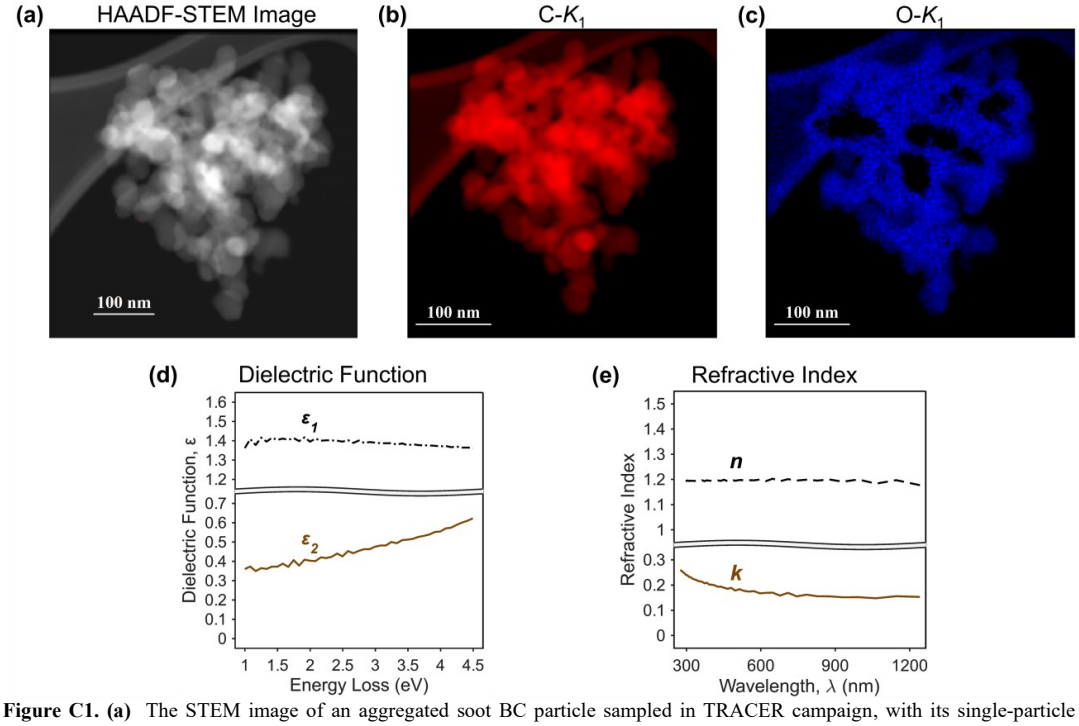

Figure C1. (a) The STEM image of an aggregated soot BC particle sampled in TRACER campaign, with its single-particle elemental composition scan showing the distribution of **(b)** carbon and **(c)** oxygen within the particle. **(d)** The real (ε_1) and imaginary (ε_2) part of the dielectric function of the aggregated soot BC particle, determined using low-loss EELS, plotted against electron energy-loss level ranging from 1 to 4 eV. **(e)** The real (n) and imaginary (k) part of the complex refractive index of the aggregated soot BC particle, derived from their dielectric function, plotted against optical wavelength ranging from 300 to 1200 nm.

https://doi.org/10.5194/egusphere-2026-4745
Preprint. Discussion started: 10 September 2026

Data Availability

All data are available in the main text or the Appendices. Data used in this study from the TRACER campaign for various instruments is available to download from the DOE ARM's Data Discovery website (https://adc.arm.gov/discovery#/).

Author Contributions

Conceptualization: YL, GSC, RKC
Methodology: YL, GSC, TSK, JVP, JK, BJS
Investigation: YL, GSC, TSK, JVP, JK, GR, JAH, ZC, NNL, GWV, BJS, CZ, DPG
Visualization: YL, GSC, TSK
Supervision: SC, RM, RKC
Writing—original draft: YL, GSC
Writing—review & editing: YL, GSC, TSK, JVP, JK, GR, JAH, ZC, NNL, GWV, BJS, CZ, DPG, SC, RM, RKC

Competing Interests

All other authors declare they have no competing interests.

Acknowledgements

All authors would like to express their gratitude to Dr. Felipe Rivera-Adorno and Dr. Alexander Laskin from the Department of Chemistry at Purdue University and Dr. Michael Jensen from Brookhaven National Laboratory for their invaluable inspiration and insightful discussions throughout this research.

Financial Support

Atmospheric System Research Program of the U.S. Department of Energy grant DE-SC0021011 (YL, GSC, TSK, JVP, JK, BJS, CZ, DPG, RKC)

Facilities Integrating Collaborations for User Science (FICUS) Program of the U.S. Department of Energy (YL, GSC, TSK, JVP, JK, BJS, CZ, DPG, RKC)

National Aeronautics and Space Administration (GR, RM)

Environmental Molecular Sciences Laboratory of the Office of Biological and Environmental Research of the U.S. Department of Energy (ZC, GWV, NNL, SC)

https://doi.org/10.5194/egusphere-2026-4745
Preprint. Discussion started: 10 September 2026

References

Adachi, K., Dibb, J. E., Katich, J. M., Schwarz, J. P., Guo, H., Campuzano-Jost, P., Jimenez, J. L., Peischl, J., Holmes, C. D., and Crawford, J.: Occurrence, abundance, and formation of atmospheric tarballs from a wide range of wildfires in the western US, Atmos. Chem. Phys., 24, 10985–11004, https://doi.org/10.5194/acp-24-10985-2024, 2024.

Adler, G., Wagner, N. L., Lamb, K. D., Manfred, K. M., Schwarz, J. P., Franchin, A., Middlebrook, A. M., Washenfelder, R. A., Womack, C. C., Yokelson, R. J., and Murphy, D. M.: Evidence in biomass burning smoke for a light-absorbing aerosol with properties intermediate between brown and black carbon, Aerosol Sci. Technol., 53, 976–989, https://doi.org/10.1080/02786826.2019.1617832, 2019.

Alexander, D. T. L., Crozier, P. A., and Anderson, J. R.: Brown Carbon Spheres in East Asian Outflow and Their Optical Properties, Science, 321, 833–836, https://doi.org/10.1126/science.1155296, 2008.

Al-Jabri, A., Lebo, Z. J., and Wang, D.: Investigating Aerosol and Meteorological Influences on Convective Clouds in Houston, Texas, during the TRACER/ESCAPE Field Campaigns, J. Atmos. Sci., 82, 2469–2489, https://doi.org/10.1175/JAS-D-25-0004.1, 2025.

Al-Naiema, I. M., Hettiyadura, A. P. S., Wallace, H. W., Sanchez, N. P., Madler, C. J., Cevik, B. K., Bui, A. A. T., Kettler, J., Griffin, R. J., and Stone, E. A.: Source apportionment of fine particulate matter in Houston, Texas: insights to secondary organic aerosols, Atmos. Chem. Phys., 18, 15601–15622, https://doi.org/10.5194/acp-18-15601-2018, 2018.

Andreae, M. O. and Gelencsér, A.: Black carbon or brown carbon? The nature of light-absorbing carbonaceous aerosols, Atmos. Chem. Phys., 6, 3131–3148, https://doi.org/10.5194/acp-6-3131-2006, 2006.

Andrews, T., Forster, P. M., Boucher, O., Bellouin, N., and Jones, A.: Precipitation, radiative forcing and global temperature change, Geophys. Res. Lett., 37, https://doi.org/10.1029/2010GL043991, 2010.

Arnott, W. P., Moosmüller, H., Rogers, C. F., Jin, T., and Bruch, R.: Photoacoustic spectrometer for measuring light absorption by aerosol: instrument description, Atmos. Environ., 33, 2845–2852, https://doi.org/10.1016/S1352-2310(98)00361-6, 1999.

Atwi, K., Cheng, Z., Hajj, O. E., Perrie, C., and Saleh, R.: A dominant contribution to light absorption by methanol-insoluble brown carbon produced in the combustion of biomass fuels typically consumed in wildland fires in the United States, Environ. Sci. Atmos., 2, 182–191, https://doi.org/10.1039/D1EA00065A, 2022.

Beeler, P. and Chakrabarty, R. K.: Disparities in PM $_{2.5}$ exposure and population density influence SARS-CoV-2 transmission among racial and ethnic minorities, Environ. Res. Lett., 16, 104046, https://doi.org/10.1088/1748-9326/ac29ea, 2021.

Bikkina, P., Bikkina, S., Kawamura, K., Sudheer, A. K., Mahesh, G., and Kumar, S. K.: Evidence for brown carbon absorption over the Bay of Bengal during the southwest monsoon season: a possible oceanic source, Environ. Sci. Process. Impacts, 22, 1743–1758, https://doi.org/10.1039/D0EM00111B, 2020.

Birch, M. E. and Cary, R. A.: Elemental carbon-based method for occupational monitoring of particulate diesel exhaust: methodology and exposure issues, The Analyst, 121, 1183, https://doi.org/10.1039/an9962101183, 1996.

Bond, T. C., Doherty, S. J., Fahey, D. W., Forster, P. M., Berntsen, T., DeAngelo, B. J., Flanner, M. G., Ghan, S., Kärcher, B., Koch, D., Kinne, S., Kondo, Y., Quinn, P. K., Sarofim, M. C., Schultz, M. G., Schulz, M., Venkataraman, C., Zhang, H., Zhang, S., Bellouin, N., Guttikunda, S. K., Hopke, P. K., Jacobson, M. Z., Kaiser, J. W., Klimont, Z., Lohmann, U., Schwarz, J. P., Shindell, D., Storelvmo, T., Warren, S. G., and Zender, C. S.: Bounding the role of black carbon in the climate system: A scientific assessment, J. Geophys. Res. Atmos., 118, 5380–5552, https://doi.org/10.1002/jgrd.50171, 2013.

https://doi.org/10.5194/egusphere-2026-4745
Preprint. Discussion started: 10 September 2026

Boreddy, S. K. R., Hegde, P., Arun, B. S., Aswini, A. R., and Babu, S. S.: Molecular composition and light-absorbing properties of organic aerosols from west-coast of tropical India, Sci. Total Environ., 845, 157163, https://doi.org/10.1016/j.scitotenv.2022.157163, 2022.

Bush, B. C. and Valero, F. P. J.: Surface aerosol radiative forcing at Gosan during the ACE-Asia campaign, J. Geophys. Res. Atmos., 108, https://doi.org/10.1029/2002JD003233, 2003.

Chakrabarty, R. K., Shetty, N. J., Thind, A. S., Beeler, P., Sumlin, B. J., Zhang, C., Liu, P., Idrobo, J. C., Adachi, K., Wagner, N. L., Schwarz, J. P., Ahern, A., Sedlacek, A. J., Lambe, A., Daube, C., Lyu, M., Liu, C., Herndon, S., Onasch, T. B., and Mishra, R.: Shortwave absorption by wildfire smoke dominated by dark brown carbon, Nat. Geosci., 16, 683–688, https://doi.org/10.1038/s41561-023-01237-9, 2023.

Clarke, A. D., Shinozuka, Y., Kapustin, V. N., Howell, S., Huebert, B., Doherty, S., Anderson, T., Covert, D., Anderson, J., Hua, X., Moore II, K. G., McNaughton, C., Carmichael, G., and Weber, R.: Size distributions and mixtures of dust and black carbon aerosol in Asian outflow: Physiochemistry and optical properties, J. Geophys. Res. Atmos., 109, https://doi.org/10.1029/2003JD004378, 2004.

Corbin, J. C. and Gysel-Beer, M.: Detection of tar brown carbon with a single particle soot photometer (SP2), Atmos. Chem. Phys., 19, 15673–15690, https://doi.org/10.5194/acp-19-15673-2019, 2019.

Corbin, J. C., Czech, H., Massabò, D., de Mongeot, F. B., Jakobi, G., Liu, F., Lobo, P., Mennucci, C., Mensah, A. A., Orasche, J., Pieber, S. M., Prévôt, A. S. H., Stengel, B., Tay, L.-L., Zanatta, M., Zimmermann, R., El Haddad, I., and Gysel, M.: Infrared-absorbing carbonaceous tar can dominate light absorption by marine-engine exhaust, Npj Clim. Atmos. Sci., 2, 12, https://doi.org/10.1038/s41612-019-0069-5, 2019.

Cosby, A. G., Lebakula, V., Smith, C. N., Wanik, D. W., Bergene, K., Rose, A. N., Swanson, D., and Bloom, D. E.: Accelerating growth of human coastal populations at the global and continent levels: 2000–2018, Sci. Rep., 14, 22489, https://doi.org/10.1038/s41598-024-73287-x, 2024.

De La Pena, F., Ostasevicius, T., Tonaas Fauske, V., Burdet, P., Jokubauskas, P., Nord, M., Sarahan, M., Prestat, E., Johnstone, D. N., Taillon, J., Jan Caron, Furnival, T., MacArthur, K. E., Eljarrat, A., Mazzucco, S., Migunov, V., Aarholt, T., Walls, M., Winkler, F., Donval, G., Martineau, B., Garmannslund, A., Zagonel, L.-F., and Iyengar, I.: Electron Microscopy (Big and Small) Data Analysis With the Open Source Software Package HyperSpy, Microsc. Microanal., 23, 214–215, https://doi.org/10.1017/S1431927617001751, 2017.

Donahue, N. M., Robinson, A. L., Stanier, C. O., and Pandis, S. N.: Coupled Partitioning, Dilution, and Chemical Aging of Semivolatile Organics, Environ. Sci. Technol., 40, 2635–2643, https://doi.org/10.1021/es052297c, 2006.

Duarte, R. M. B. O. and Duarte, A. C.: Urban Atmospheric Aerosols: Sources, Analysis, and Effects, Atmosphere, 11, 1221, https://doi.org/10.3390/atmos11111221, 2020.

Egerton, R.: Electron Energy Loss Spectroscopy in the TEM, Rep. Prog. Phys. Rep Prog Phys, 72, 16502–25, https://doi.org/10.1088/0034-4885/72/1/016502, 2009.

Emde, C., Buras-Schnell, R., Kylling, A., Mayer, B., Gasteiger, J., Hamann, U., Kylling, J., Richter, B., Pause, C., Dowling, T., and Bugliaro, L.: The libRadtran software package for radiative transfer calculations (version 2.0.1), Geosci. Model Dev., 9, 1647–1672, https://doi.org/10.5194/gmd-9-1647-2016, 2016.

Farley, R., Lee, J., Rivellini, L.-H., Lee, A., Dal Porto, R., Cappa, C., Gorkowski, K., Shawon, A. S. M., Benedict, K., Aiken, A., Dubey, M., and Zhang, Q.: Chemical Properties and Single Particle Mixing State of Soot Aerosol in Houston during the TRACER Campaign, EGUsphere, 1–33, https://doi.org/10.5194/egusphere-2023-2328, 2023.

Fast, J. D., Gustafson Jr., W. I., Easter, R. C., Zaveri, R. A., Barnard, J. C., Chapman, E. G., Grell, G. A., and Peckham, S. E.: Evolution of ozone, particulates, and aerosol direct radiative forcing in the vicinity of Houston using a fully

https://doi.org/10.5194/egusphere-2026-4745
Preprint. Discussion started: 10 September 2026

coupled meteorology-chemistry-aerosol model, J. Geophys. Res. Atmos., 111, https://doi.org/10.1029/2005JD006721, 2006.

Gliß, J., Mortier, A., Schulz, M., Andrews, E., Balkanski, Y., Bauer, S. E., Benedictow, A. M. K., Bian, H., Checa-Garcia, R., Chin, M., Ginoux, P., Griesfeller, J. J., Heckel, A., Kipling, Z., Kirkevåg, A., Kokkola, H., Laj, P., Le Sager, P., Lund, M. T., Lund Myhre, C., Matsui, H., Myhre, G., Neubauer, D., van Noije, T., North, P., Olivié, D. J. L., Rémy, S., Sogacheva, L., Takemura, T., Tsigaridis, K., and Tsyro, S. G.: AeroCom phase III multi-model evaluation of the aerosol life cycle and optical properties using ground- and space-based remote sensing as well as surface in situ observations, Atmos. Chem. Phys., 21, 87–128, https://doi.org/10.5194/acp-21-87-2021, 2021.

Guagenti, M., Shrestha, S., Mehra, M., Yoon, S., Ramirez, M. T. S., Iii, J. H. F., and Usenko, S.: Temporal Profiles of Volatile Organic Compounds near the Houston Ship Channel, Texas, Atmosphere, 16, https://doi.org/10.3390/atmos16030260, 2025.

Hoffer, A., Tóth, A., Nyirő-Kósa, I., Pósfai, M., and Gelencsér, A.: Light absorption properties of laboratory-generated tar ball particles, Atmos. Chem. Phys., 16, 239–246, https://doi.org/10.5194/acp-16-239-2016, 2016.

Hoffer, A., Tóth, Á., Pósfai, M., Chung, C. E., and Gelencsér, A.: Brown carbon absorption in the red and near-infrared spectral region, Atmos. Meas. Tech., 10, 2353–2359, https://doi.org/10.5194/amt-10-2353-2017, 2017.

Huang, R.-J., Yang, L., Cao, J., Chen, Y., Chen, Q., Li, Y., Duan, J., Zhu, C., Dai, W., Wang, K., Lin, C., Ni, H., Corbin, J. C., Wu, Y., Zhang, R., Tie, X., Hoffmann, T., O'Dowd, C., and Dusek, U.: Brown Carbon Aerosol in Urban Xi'an, Northwest China: The Composition and Light Absorption Properties, Environ. Sci. Technol., 52, 6825–6833, https://doi.org/10.1021/acs.est.8b02386, 2018.

Idrobo, J. C. and Zhou, W.: A short story of imaging and spectroscopy of two-dimensional materials by scanning transmission electron microscopy, Ultramicroscopy, 180, 156–162, https://doi.org/10.1016/j.ultramic.2017.02.002, 2017.

Intergovernmental Panel On Climate Change: Climate Change 2021 – The Physical Science Basis: Working Group I Contribution to the Sixth Assessment Report of the Intergovernmental Panel on Climate Change, 1st ed., Cambridge University Press, https://doi.org/10.1017/9781009157896, 2023.

Jensen, M. P., Flynn, J. H., Judd, L. M., Kollias, P., Kuang, C., Mcfarquhar, G., Nadkarni, R., Powers, H., and Sullivan, J.: A Succession of Cloud, Precipitation, Aerosol, and Air Quality Field Experiments in the Coastal Urban Environment, Bull. Am. Meteorol. Soc., 103, 103–105, https://doi.org/10.1175/BAMS-D-21-0104.1, 2022.

Jensen, M. P., Flynn, J. H., Gonzalez-Cruz, J. E., Judd, L. M., Kollias, P., Kuang, C., McFarquhar, G. M., Powers, H., Ramamurthy, P., Sullivan, J., Aiken, A. C., Alvarez, S. L., Argay, P., Argrow, B., Bell, T. M., Boyer, D., Brooks, S. D., Bruning, E. C., Brunner, K., Butterworth, B., Calmer, R., Cappa, C. D., Chakrabarty, R. K., Chandrasekar, V., Chao, C.-Y., Chen, B., China, S., Collins, D. R., Collis, S. M., Crowell, S., Porto, R. D., Boer, G. de, Deng, M., Dexheimer, D., Drager, A. J., Du, X., Dubey, M. K., Dzambo, A. M., Etten-Bohm, M., Fan, J., Farley, R., Feng, Y.-C., Feng, Y., Fenn, M., Ferrare, R. E., Flusche, S., Fridlind, A. M., Galewsky, J., Gamarro, H., Gardner, S., Ghate, V. P., Giangrande, S. E., Griffin, R. J., Griggs, T., Gronoff, G. P., Grover, M., Gaugenti, M., Guo, F., Gupta, S., Hu, J., Huang, Y., Jackson, R. C., Hair, J. W., Johnson, K. L., Kasparoglu, S., Klein, P., Kotsakis, A. E., Kumar, J., Kumjian, M. R., Lamer, K., Lappin, F. M., Lei, Z., Li, J., Li, R., Li, Y., Logan, T., Lombardo, K., Luke, E. P., Mages, Z., Matthews, A. A., Matthews, B. H., Mayol-Bracero, O., Matsui, T., McKeown, K. E., Mehra, M., Mei, F., Meskidzhe, N., Nguyen, C., Nielsen, E. R., Nowotarski, C. J., Oaks, D., Oktem, R., Oue, M., Park, J. M., Partida, N., Patil, S., Pena, J. C., Petters, M. D., Phoenix, D. B., et al.: Studying Aerosol, Clouds, and Air Quality in the Coastal Urban Environment of Southeastern Texas, https://doi.org/10.1175/BAMS-D-23-0331.1, 2025.

Kim, H., Kim, J. Y., Jin, H. C., Lee, J. Y., and Lee, S. P.: Seasonal variations in the light-absorbing properties of water-soluble and insoluble organic aerosols in Seoul, Korea, Atmos. Environ., 129, 234–242, https://doi.org/10.1016/j.atmosenv.2016.01.042, 2016.

https://doi.org/10.5194/egusphere-2026-4745
Preprint. Discussion started: 10 September 2026

Kirchstetter, T. W., Novakov, T., and Hobbs, P. V.: Evidence that the spectral dependence of light absorption by aerosols is affected by organic carbon, J. Geophys. Res. Atmos., 109, https://doi.org/10.1029/2004JD004999, 2004.

Lamer, K., Mages, Z., Treserras, B. P., Walter, P., Zhu, Z., Rapp, A. D., Nowotarski, C. J., Brooks, S. D., Flynn, J., Sharma, M., Klein, P., Spencer, M., Smith, E., Gebauer, J., Bell, T., Bunting, L., Griggs, T., Wagner, T. J., and McKeown, K.: Spatially distributed atmospheric boundary layer properties in Houston – A value-added observational dataset, Sci. Data, 11, 661, https://doi.org/10.1038/s41597-024-03477-9, 2024.

Laskin, A., Iedema, M. J., and Cowin, J. P.: Time-Resolved Aerosol Collector for CCSEM/EDX Single-Particle Analysis, Aerosol Sci. Technol., 37, 246–260, https://doi.org/10.1080/02786820300945, 2003a.

Laskin, A., Iedema ,Martin J., and and Cowin, J. P.: Time-Resolved Aerosol Collector for CCSEM/EDX Single-Particle Analysis, Aerosol Sci. Technol., 37, 246–260, https://doi.org/10.1080/02786820300945, 2003b.

Laskin, A., Laskin, J., and Nizkorodov, S. A.: Chemistry of Atmospheric Brown Carbon, Chem. Rev., 115, 4335–4382, https://doi.org/10.1021/cr5006167, 2015.

Lei, Y., Shen, Z., Wang, Q., Zhang, T., Cao, J., Sun, J., Zhang, Q., Wang, L., Xu, H., Tian, J., and Wu, J.: Optical characteristics and source apportionment of brown carbon in winter PM2.5 over Yulin in Northern China, Atmos. Res., 213, 27–33, https://doi.org/10.1016/j.atmosres.2018.05.018, 2018.

Ma, J., Li, X., Gu, P., Dallmann, T. R., Presto, A. A., and Donahue, N. M.: Estimating ambient particulate organic carbon concentrations and partitioning using thermal optical measurements and the volatility basis set, Aerosol Sci. Technol., 50, 638–651, https://doi.org/10.1080/02786826.2016.1158778, 2016.

MacManus, K., Balk, D., Engin, H., McGranahan, G., and Inman, R.: Estimating population and urban areas at risk of coastal hazards, 1990–2015: how data choices matter, Earth Syst. Sci. Data, 13, 5747–5801, https://doi.org/10.5194/essd-13-5747-2021, 2021.

Moosmüller, H., Chakrabarty, R. K., and Arnott, W. P.: Aerosol light absorption and its measurement: A review, J. Quant. Spectrosc. Radiat. Transf., 110, 844–878, https://doi.org/10.1016/j.jqsrt.2009.02.035, 2009.

Navinya, C., Kapoor, T. S., Anurag, G., Venkataraman, C., Phuleria, H. C., and Chakrabarty, R. K.: Brownness of organics in anthropogenic biomass burning aerosols over South Asia, Atmos. Chem. Phys., 24, 13285–13297, https://doi.org/10.5194/acp-24-13285-2024, 2024.

Navinya, C., Kapoor, T. S., Venkataraman, C., Phuleria, H. C., and Chakrabarty, R. K.: Brown Carbon Light Absorption over India: Research Status and Need for Discerning Climate Impacts, ACS EST Air, 2, 1115–1135, https://doi.org/10.1021/acsestair.5c00010, 2025.

Ramanathan, V. and Carmichael, G.: Global and regional climate changes due to black carbon, Nat. Geosci., 1, 221–227, https://doi.org/10.1038/ngeo156, 2008.

Rathod, T. D., Sahu, S. K., Tiwari, M., Bhangare, R. C., and Ajmal, P. Y.: Optical properties of water soluble and organic soluble carbonaceous aerosols at an urban location in India, Atmos. Pollut. Res., 15, 101956, https://doi.org/10.1016/j.apr.2023.101956, 2024.

Saleh, R.: From Measurements to Models: Toward Accurate Representation of Brown Carbon in Climate Calculations, Curr. Pollut. Rep., 6, 90–104, https://doi.org/10.1007/s40726-020-00139-3, 2020.

Saleh, R., Robinson, E. S., Tkacik, D. S., Ahern, A. T., Liu, S., Aiken, A. C., Sullivan, R. C., Presto, A. A., Dubey, M. K., Yokelson, R. J., Donahue, N. M., and Robinson, A. L.: Brownness of organics in aerosols from biomass burning linked to their black carbon content, Nat. Geosci., 7, 647–650, https://doi.org/10.1038/ngeo2220, 2014.

https://doi.org/10.5194/egusphere-2026-4745
Preprint. Discussion started: 10 September 2026

Saleh, R., Cheng, Z., and Atwi, K.: The Brown–Black Continuum of Light-Absorbing Combustion Aerosols, Environ. Sci. Technol. Lett., 5, 508–513, https://doi.org/10.1021/acs.estlett.8b00305, 2018.

Sand, M., Samset, B. H., Myhre, G., Gliß, J., Bauer, S. E., Bian, H., Chin, M., Checa-Garcia, R., Ginoux, P., Kipling, Z., Kirkevåg, A., Kokkola, H., Le Sager, P., Lund, M. T., Matsui, H., van Noije, T., Olivié, D. J. L., Remy, S., Schulz, M., Stier, P., Stjern, C. W., Takemura, T., Tsigaridis, K., Tsyro, S. G., and Watson-Parris, D.: Aerosol absorption in global models from AeroCom phase III, Atmos. Chem. Phys., 21, 15929–15947, https://doi.org/10.5194/acp-21-15929-2021, 2021.

Schwarz, J. P., Stark, H., Spackman, J. R., Ryerson, T. B., Peischl, J., Swartz, W. H., Gao, R. S., Watts, L. A., and Fahey, D. W.: Heating rates and surface dimming due to black carbon aerosol absorption associated with a major U.S. city, Geophys. Res. Lett., 36, https://doi.org/10.1029/2009GL039213, 2009.

Schwarz, M., Folini, D., Yang, S., Allan, R. P., and Wild, M.: Changes in atmospheric shortwave absorption as important driver of dimming and brightening, Nat. Geosci., 13, 110–115, https://doi.org/10.1038/s41561-019-0528-y, 2020.

Shetty, N. J., Pandey, A., Baker, S., Hao, W. M., and Chakrabarty, R. K.: Measuring light absorption by freshly emitted organic aerosols: optical artifacts in traditional solvent-extraction-based methods, Atmos. Chem. Phys., 19, 8817–8830, https://doi.org/10.5194/acp-19-8817-2019, 2019.

Simoneit, B. R. T., Kobayashi, M., Mochida, M., Kawamura, K., Lee, M., Lim, H.-J., Turpin, B. J., and Komazaki, Y.: Composition and major sources of organic compounds of aerosol particulate matter sampled during the ACE-Asia campaign, J. Geophys. Res. Atmos., 109, https://doi.org/10.1029/2004JD004598, 2004.

Sumlin, B. J., Heinson, W. R., and Chakrabarty, R. K.: Retrieving the aerosol complex refractive index using PyMieScatt: A Mie computational package with visualization capabilities, J. Quant. Spectrosc. Radiat. Transf., 205, 127–134, https://doi.org/10.1016/j.jqsrt.2017.10.012, 2018.

Thompson, S. A., Chen, B., Matthews, B. H., Li, R., Nowotarski, C. J., Rapp, A. D., and Brooks, S. D.: Characterizing Greater Houston's Aerosol by Air Mass During TRACER, J. Geophys. Res. Atmos., 130, e2025JD043353, https://doi.org/10.1029/2025JD043353, 2025.

Wang, X., Chakrabarty, R. K., Schwarz, J. P., Murphy, S. M., Levin, E. J. T., Howell, S. G., Guo, H., Campuzano-Jost, P., and Jimenez, J. L.: Dark brown carbon from biomass burning contributes to significant global-scale positive forcing, One Earth, 8, https://doi.org/10.1016/j.oneear.2025.101205, 2025.

Wild, M.: Global dimming and brightening: A review, J. Geophys. Res. Atmos., 114, https://doi.org/10.1029/2008JD011470, 2009.

Wu, C., Wu, D., and Yu, J. Z.: Quantifying black carbon light absorption enhancement with a novel statistical approach, Atmos. Chem. Phys., 18, 289–309, https://doi.org/10.5194/acp-18-289-2018, 2018.

Yan, C., Zheng, M., Bosch, C., Andersson, A., Desyaterik, Y., Sullivan, A. P., Collett, J. L., Zhao, B., Wang, S., He, K., and Gustafsson, Ö.: Important fossil source contribution to brown carbon in Beijing during winter, Sci. Rep., 7, 43182, https://doi.org/10.1038/srep43182, 2017.

Zeng, L., Zhang, A., Wang, Y., Wagner, N. L., Katich, J. M., Schwarz, J. P., Schill, G. P., Brock, C., Froyd, K. D., Murphy, D. M., Williamson, C. J., Kupc, A., Scheuer, E., Dibb, J., and Weber, R. J.: Global Measurements of Brown Carbon and Estimated Direct Radiative Effects, Geophys. Res. Lett., 47, e2020GL088747, https://doi.org/10.1029/2020GL088747, 2020.

Zhang, W., Villarini, G., Vecchi, G. A., and Smith, J. A.: Urbanization exacerbated the rainfall and flooding caused by hurricane Harvey in Houston, Nature, 563, 384–388, https://doi.org/10.1038/s41586-018-0676-z, 2018.

https://doi.org/10.5194/egusphere-2026-4745
Preprint. Discussion started: 10 September 2026

792 Zhang, X., Lin, Y.-H., Surratt, J. D., Zotter, P., Prévôt, A. S. H., and Weber, R. J.: Light-absorbing soluble organic
793 aerosol in Los Angeles and Atlanta: A contrast in secondary organic aerosol, Geophys. Res. Lett., 38,
794 https://doi.org/10.1029/2011GL049385, 2011.

795 Zhang, X., Lin, Y.-H., Surratt, J. D., and Weber, R. J.: Sources, Composition and Absorption Ångström Exponent of
796 Light-absorbing Organic Components in Aerosol Extracts from the Los Angeles Basin, Environ. Sci. Technol., 47,
797 3685–3693, https://doi.org/10.1021/es305047b, 2013.

798 Zhu, J., Crozier, P. A., Ercius, P., and Anderson, J. R.: Derivation of Optical Properties of Carbonaceous Aerosols by
799 Monochromated Electron Energy-Loss Spectroscopy, Microsc. Microanal., 20, 748–759,
800 https://doi.org/10.1017/S143192761400049X, 2014.

801